Journal of Thermal Stresses, 28: 747–782, 2005

ISSN: 0149-5739 print/1521-074X online
DOI: 10.1080/01495730590932724

Taylor & Francis
Taylor & Francis Group

Sixth International Congress on Thermal Stresses, TS 2005, Vienna, May 26–29, 2005
Ernst Melan & Heinz Parkus Memorial Session

MESOSCALE ANALYSIS OF SHEAR BANDS IN HIGH STRAIN RATE DEFORMATIONS OF TUNGSTEN/NICKEL-IRON COMPOSITES

R. C. Batra and B. M. Love
Department of Engineering Science and Mechanics, Virginia Polytechnic Institute and State University, Blacksburg, Virginia, USA

We analyze the initiation and propagation of adiabatic shear bands in a tungsten heavy alloy by modeling each constituent as a heat-conducting, microporous, isotropic, elastothermoviscoplastic material. The two constituents are assumed to be perfectly bonded to each other so that the temperature, heat flux, displacements, and surface tractions are continuous across an interface between a tungsten particulate and the nickel-iron matrix. Three different modes of deformation, namely plane strain tension/compression, plane strain shear, and axisymmetric tension/compression are analyzed. No other defects are introduced. It is found that contours of the rate of temperature rise and/or velocity and/or the specific energy dissipation rate rather than those of effective plastic strain delineate the shear banded regions. For the same volume fraction of particulates smaller diameter particulates enhance the formation of adiabatic shear bands. The time of initiation of an adiabatic shear band also depends upon the particulate arrangement.

Keywords: Mesoscale analysis; Finite element solution; Thermoviscoplasticity; Microporous materials; Particulate composite; Tungsten heavy alloys

An adiabatic shear band (ASB) is a narrow region, usually a few μm wide, of intense plastic deformation that forms in most materials deformed at high strain rates. Even though heat conduction plays a significant role during the development of an ASB, it is termed adiabatic since there is not enough time for the heat to be conducted away from the shear banded region. The analysis of ASBs is important because they precede ductile fracture and play an important role in penetration problems. Even though the initiation, development and propagation of ASBs have been extensively

Received 2 February 2005; accepted 9 February 2005.
This work was partially supported by the NSF grant CMS0002849, the ONR grants N00014-98-1-0300 and N00014-03-MP-2-0131, the ARO grant DAAD19-01-1-0657 and the AFOSR MURI to Georgia Institute of Technology with a subcontract to Virginia Polytechnic Institute and State University. Views expressed in the paper are those of authors and not of funding agencies.
Address correspondence to R. C. Batra, Department of Engineering Science and Mechanics, MC 0219, Virginia Polytechnic Institute and State University, Blacksburg, VA 24061, USA. E-mail: rbatra@vt.edu

studied in homogeneous materials, (e.g., see the two books by Bai and Dodd [1] and Wright [2], the two volumes edited by Perzyna [3] and Batra and Zbib [4], the review paper of Tomita [5], and special issues of three journals edited by Armstrong et al. [6], Batra et al. [7], and Zbib et al. [8]), there are very few studies on ASBs in particulate composites.

Pressure/shear plate impact experiments on a tungsten heavy alloy (WHA) have shown that the two-phase composite is more susceptible to adiabatic shear banding than either one of its constituents [9,10]; a similar conclusion was drawn in [11]. Bose et al. [12], Kim et al. [13], and Wei et al. [14] have scrutinized the influence of microstructural details, such as the particulate shape and size, the volume fraction of particulates, and their predeformation on the ASB formation in WHAs. Dick et al. [15] have performed reverse ballistic tests on cylindrical rods of WHAs. They found that an ASB originated from a point on the rod's mantle where the mushroomed head transitioned into the cylindrical portion, and propagated inwards. Tungsten grains in the path of the ASB were severely distorted. Stevens and Batra [16] have analyzed, by the finite element method (FEM), transient thermomechanical deformations of a rapidly moving cylindrical WHA rod striking a stationary smooth rigid flat surface. They modeled the rod material as homogeneous and isotropic, and found that enhanced thermal softening of the material resulted in the formation of ASBs at approximately the same location as that observed by Dick et al. [15]. Batra and Stevens [17] have also compared the deformations of WHA and depleted uranium rods penetrating into a rolled homogeneous armor plate with each material modeled as homogeneous, isotropic, and thermoviscoplastic. Batra and Wilson [18] studied plane strain thermomechanical deformations of a WHA specimen with rectangular NiFe particles randomly distributed in and perfectly bonded to the W matrix.

Zhou [19] used the FEM to study ASBs in transient coupled thermomechanical simple shearing deformations of a heat-conducting WHA containing circular W particulates perfectly bonded to the NiFe matrix. An ASB initiated from a notch tip introduced to simulate the collective effect of numerous microvoids and other defects that may be present in a WHA. For a particulate composite replaced by an equivalent inhomogeneous thermoviscoplastic body Batra and Love [9] and Charalambakis and Baxevanis [20] have studied the localization of deformation into ASBs. These works assumed that the material properties vary continuously in the body.

The analysis of ASBs in particulate composites is very challenging because of the presence of numerous interfaces between the particulates and the matrix. The mismatch between the thermomechanical properties of the constituents introduces a discontinuity in the gradients of deformation and temperature. In a transient problem it also results in the reflection and refraction of waves. For perfectly bonded interfaces, the strength of the discontinuity depends upon the mismatch between the values of thermophysical constants of the two materials, and the particulate shape and size. An equally challenging issue is the criterion for the initiation of an ASB. In a homogeneous material, an ASB is assumed to initiate at a point when the maximum shear stress there has dropped to 80% of its peak value at that point and the material point is deforming plastically. However, in a particulate composite even when the deformation has begun to localize at a point, the material surrounding it may resist its propagation resulting in either that material point failing or in the redistribution of the load and possibly delaying the onset of an ASB.

Here we analyze transient plane strain and axisymmetric coupled thermomechanical deformations of a heat-conducting microporous WHA, presume that W particulates are randomly distributed in the NiFe matrix, and are both in perfect mechanical and thermal contact with the matrix. Numerous inhomogeneities in deformation introduced by the tungsten/matrix interfaces interact with each other to determine when and where ASBs initiate. Three modes of deformation namely plane strain tension/compression, plane strain simple shear, and axisymmetric compression are analyzed.

The paper is organized as follows. Next, we give the governing equations, initial and boundary conditions, interface conditions, semi-discrete formulation of the problem, values of material parameters, the ASB initiation criterion in a homogeneous body and various length and time scales in the problem. Following that, we describe briefly the computer code, how it is verified, and the effect of the FE mesh on the ASB initiation time. Then, we describe and discuss results for the particulate composite. Effects of particulate size, particulate arrangement, and volume fraction of particulates are studied. An equivalent homogeneous body with initial porosity distribution is found so that an ASB will initiate at about the same time in the homogenized body and the particulate composite. The conclusions of this study are summarized near the end of the paper.

FORMULATION OF THE PROBLEM

Governing Equations

We assume that the particulate and the matrix materials can be modeled as isotropic, microporous, and elastothermoviscoplastic. We use rectangular Cartesian coordinates and the referential description of motion to describe their finite two-dimensional transient coupled thermomechanical deformations. Plane strain tensile, plane strain compressive, plane strain simple shear, and axisymmetric deformations are analyzed. Deformations of each constituent and the composite body are governed by Eqs. (1)–(4) expressing, respectively, the balance of mass, the balance of linear momentum, the balance of moment of momentum, and the balance of internal energy.

$$\rho(1-f)J = \rho_0(1-f_0) \tag{1}$$

$$\rho_0(1-f_0)\dot{v}_i = T_{i\alpha,\alpha},\ i,j = 1,2,3,\ \alpha = 1,2,3 \tag{2}$$

$$T_{i\alpha}F_{j\alpha} = T_{j\alpha}F_{i\alpha} \tag{3}$$

$$\rho_0(1-f_0)\dot{e} = -Q_{\alpha,\alpha} + T_{i\alpha}\dot{F}_{i\alpha} \tag{4}$$

Here ρ is the present mass density, f the porosity (i.e., the volume fraction of voids), $J = \det \mathbf{F}$, $F_{i\alpha} = x_{i,\alpha} = \partial x_i/\partial X_\alpha$ the deformation gradient, $\mathbf{x}$ the present position at time t of a material particle located at the place $\mathbf{X}$ in the reference configuration, $\mathbf{T}$ the first Piola–Kirchhoff stress tensor, e the specific internal energy, $\mathbf{Q}$ the present heat flux measured per unit reference area, $\mathbf{v}$ the velocity of a material particle, a superimposed dot indicates the material time derivative, and a repeated index implies

summation over the range of the index. Greek indices refer to coordinates in the reference configuration, and Latin indices to coordinates in the present configuration. The porosity f is assumed to be uniformly distributed in each constituent, and can be regarded as a measure of the damage.

We assume that the strain-rate tensor $\mathbf{D}$ defined by $D_{ij} = (v_{i,j} + v_{j,i})/2$, $v_{i,j} = \partial v_i/\partial x_j$, has the additive decomposition into an elastic part $\mathbf{D}^e$, a plastic part $\mathbf{D}^p$ and a thermal part $\hat{\alpha}\dot{\theta}\mathbf{1}$, viz., $\mathbf{D} = \mathbf{D}^e + \mathbf{D}^p + \hat{\alpha}\dot{\theta}\mathbf{1}$. Here $\hat{\alpha}$ is the coefficient of thermal expansion, θ the temperature rise, and $\mathbf{1}$ the identity tensor. Second-order tensors $\mathbf{D}^e$ and $\mathbf{D}^p$ are presumed to be objective or frame-indifferent. Eqs. (1)–(4) are supplemented with the following constitutive relations.

$$\dot{\sigma}_{ij} + \sigma_{ik}W_{kj} + \sigma_{jk}W_{ki} = \frac{E(1-f)}{1+\nu}D^e_{ij} + \frac{E(1-f)\nu}{(1+\nu)(1-2\nu)}D^e_{kk}\delta_{ij} \tag{5}$$

$$\dot{e} = c\tau\ddot{\theta} + c\dot{\theta} + \frac{1}{\rho(1-f)}\sigma_{ij}D^e_{ij}, \;\; T_{i\alpha} = J\sigma_{ij}(F^{-1})_{\alpha j} \tag{6}$$

$$q_i = -\kappa\left(1 - \frac{3}{2}f\right)\theta_{,i}, \;\; Q_\alpha = Jq_i(F^{-1})_{\alpha i} \tag{7}$$

$$\phi \equiv \frac{\sigma_e^2}{\sigma_y^2} - 1 + 2f^*\beta_1\cosh\left(\frac{3\beta_2\bar{p}}{2\sigma_y}\right) - \beta_1^2(f^*)^2 = 0, \;\; \sigma_e^2 = \frac{3}{2}\sigma'_{ij}\sigma'_{ij}, \quad i,j = 1,2,3 \tag{8}$$

$$D^p_{ij} = \dot{\lambda}\frac{\partial\phi}{\partial\sigma_{ij}} = \dot{\lambda}\left[\frac{3\sigma'_{ij}}{\sigma_y^2} - \frac{f^*\beta_1\beta_2}{\sigma_y}\sinh\left(\frac{3\beta_2\bar{p}}{2\sigma_y}\right)\delta_{ij}\right], \quad \sigma'_{ij} = \sigma_{ij} + p\delta_{ij} \tag{9}$$

$$p = -(\sigma_{11} + \sigma_{22} + \sigma_{33})/3, \;\; \bar{p} = pH(-p-0) \tag{10}$$

$$\dot{\lambda} = \begin{cases} \dfrac{(1-f)\sigma_y\dot{\varepsilon}^p_e}{\sigma_{ij}\frac{\partial\phi}{\partial\sigma_{ij}}}, & \text{if } \phi = 0 \text{ and } \dot{\phi} \geq 0 \\ 0 & \text{when either } \phi < 0 \text{ or } \phi = 0 \text{ and } \dot{\phi} < 0 \end{cases} \tag{11}$$

$$\dot{f} = (1-f)D^p_{ii} + \frac{f_2\dot{\varepsilon}^p_e}{s_2\sqrt{2\pi}}\, e^{-\frac{1}{2}\left(\frac{\varepsilon^p_e - \varepsilon_n}{s_2}\right)^2} H(-p-0) \tag{12}$$

$$f^* = \begin{cases} f, \; f \leq f_c \\ f_c + \dfrac{f_u - f_c}{f_f - f_c}(f - f_c), \; f > f_c \end{cases} \tag{13}$$

$$\sigma_y = (A + B(\varepsilon^p_e)^n)\left(1 + \tilde{C}\ln\left(\frac{\dot{\varepsilon}^p_e}{\dot{\varepsilon}^p_0}\right)\right)\left(1 - \left(\frac{\theta - \theta_r}{\theta_m - \theta_r}\right)^m\right) \tag{14}$$

The left-hand side of Eq. (5) equals the Jaumann derivative of the Cauchy stress tensor $\boldsymbol{\sigma}$, $W_{ij} = (v_{i,j} - v_{j,i})/2$ is the spin tensor, E Young's modulus, ν Poisson's ratio,

c the specific heat, τ the thermal relaxation time, κ the thermal conductivity of the solid material, and θ the present temperature of a material particle. Constitutive relation (5) implies that each constituent is being modeled as an isotropic hypoelastic material. Replacing the Jaumann derivative of $\boldsymbol{\sigma}$ by another objective stress rate will change the constitutive description of the material. However, Batra and Jaber [21] found that it does not alter the ASB initiation time in a homogeneous thermoviscoplastic material. $\phi = 0$ describes the yield surface proposed by Gurson [22] for a porous material, p is the hydrostatic pressure, and f^* the modified value of porosity given by Eq. (13).

Gurson's yield surface is based on quasistatic analysis with the matrix material modeled as rigid perfectly plastic and obeying von Mises yield criterion. Constants β_1 and β_2, introduced by Tvergaard [23], provide a better fit of results computed from a FE analysis of the formation of ASBs in a plate having an array of large cylindrical voids with test observations, and $\dot{\lambda}$ is the factor of proportionality defined by Eq. (11); $\dot{\lambda} > 0$ only when the material point is deforming plastically. σ_y is the current yield stress of the material whose dependence upon the effective plastic strain ε_e^p, the effective plastic strain rate $\dot{\varepsilon}_e^p$ and the temperature θ is described by the Johnson–Cook [24] relation (14) in which $A,\ B,\ \tilde{C},\ \dot{\varepsilon}_0^p$, and m are material parameters, θ_r the room temperature, and θ_m the melting temperature of the material. Parameters B and n characaterize the strain hardening of the material, $\tilde{C}$ and $\dot{\varepsilon}_0^p$ the strain-rate hardening and the last factor on the right-hand side of Eq. (14) its thermal softening.

Eq. (12) gives the evolution of porosity; the first term on its right-hand side is derived by assuming that the matrix is incompressible and the elastic dilatation is negligible as compared to the plastic dilatation, and the second term is the strain based nucleation of voids introduced by Chu and Needleman [25]. $f_2,\ s_2$, and ε_n are material parameters; the rate of nucleation of voids is highest when ε_e^p equals ε_n and decays exponentially with the difference between ε_e^p and ε_n. H is the Heaviside step function. We have thus assumed that new voids nucleate only when the hydrostatic stress is tensile. To account for the coalescence of neighboring voids, Tvergaard and Needleman [26] enhanced the porosity, as given by Eq. (13), after it reaches its critical value f_c. In Eq. (13), f_f is the porosity at ductile fracture, and $f_u = 1/\beta_1$ is the porosity when the yield surface has shrunk to a point. Eqs. (8) and (14) imply that the radius of the von Mises yield surface increases due to strain- and strain-rate hardening of the material but decreases due to the softening induced by the temperature rise and the increase in porosity. The degradation of material properties due to the damage, taken here synonymous with the porosity, is indicated by Eqs. (5) through (8). The expression for the thermal conductivity in Eq. $(7)_1$ is due to Budiansky [27].

Substitution from Eqs. $(6)_1$ and (7) into (4) gives the following hyperbolic heat equation:

$$\rho_0(1-f_0)c(\tau\ddot{\theta}+\dot{\theta}) = \left(\kappa\left(1-\frac{3}{2}f\right)\theta_{,\alpha}\right)_{,\alpha} + J\sigma_{ij}D_{ij}^p \tag{15}$$

The term $J\sigma_{ij}D_{ij}^p$ equals the heating due to plastic working per unit volume in the reference configuration; thus the Taylor-Quinney parameter has been taken as 1. Except for a delay in the time of initiation of an ASB other results remain

unaffected by a lower value of the Taylor-Quinney factor. The form (15) of the hyperbolic heat equation is due to Cattaneo [28] and Vernotte [29]. The thermal relaxation time τ in it represents the time required to establish a steady state of heat conduction in an element suddenly exposed to heat flux. For a typical steel, $\tau = 1 \times 10^{-12}$ s, and $\tau \simeq 25 \times 10^{-12}$ s for copper. Batra and Lear [30] and Batra and Chen [31] found that the finiteness of the thermal wave speed affects the ASB initiation time in a typical steel and the spacing between adjacent shear bands only when $\tau \geq 10^{-6}$ s. Batra [32] considered higher-order spatial and temporal gradients of temperature and derived a heat equation that admits finite speeds of thermal waves. However, in such a material either a thermal wave propagates with a finite speed or the linearized problem has a unique solution. Ideally, one will like to have both.

We note that Batra and Kim [33], Batra and Jaber [21], and Batra and Chen [31,34] have analyzed different aspects of shear banding with four different thermoviscoplastic relations, namely, the Johnson–Cook [24], the Litonski–Batra (e.g., Batra [35]), the Bodner–Partom [36], and a power law. These relations were calibrated to give nearly the same effective stress vs. the effective strain curve during homogeneous deformations of the body. However, during inhomogeneous deformations, each one of the relations gave qualitatively similar but quantitatively different results. The decision to use the Johnson–Cook relation here is based on the availability of values of thermomechanical parameters for tungsten and nickel-iron.

Initial and Boundary Conditions

Each constituent is initially at rest, stress free, at a uniform temperature, has zero rate of change of temperature, and a prescribed initial porosity. Thus

$$\begin{aligned} &\mathbf{x}(\mathbf{X},0) = \mathbf{X},\ \mathbf{v}(\mathbf{X},0) = \mathbf{0},\ \theta(\mathbf{X},0) = \theta_0,\ \dot{\theta}(\mathbf{X},0) = 0,\ \rho(\mathbf{X},0) = \rho_0(\mathbf{X}),\ \boldsymbol{\sigma}(\mathbf{X},0) = \mathbf{0} \\ &\varepsilon_e^p(\mathbf{X},0) = 0,\ f(\mathbf{X},0) = f_0(\mathbf{X}),\ \mathbf{X} \in \Omega \end{aligned} \tag{16}$$

Here Ω is the region occupied by the body in the reference configuration.

When analyzing plane strain tensile deformations, the body is assumed to be prismatic having a uniform cross-section in the X_1X_2-plane, and the volume fractions of constituents, initial conditions, and boundary conditions are taken to be independent of the X_3-coordinate; e.g., see Figure 1a. Furthermore, the cross-section is a square of side $2H$, and thermomechanical deformations are assumed to be symmetric about the two centroidal axes. Thus the compositional profile has been tacitly assumed to be symmetric about the two centroidal axes. Boundary conditions $(17)_{4-6}$ and $(17)_{7-9}$, listed below, arising from the symmetry of deformations are imposed at points on the centroidal axes $X_1 = 0$ and $X_2 = 0$. The vertical surface $X_1 = H$ is taken to be traction free and thermally insulated; see Eq. $(17)_{1-3}$. Normal velocity, null tangential tractions, and zero heat flux are prescribed on the top horizontal surface $X_2 = H$; these are given by Eq. $(17)_{10-12}$. The prescribed normal velocity, given by Eq. $(17)_{12}$, increases linearly with time to its steady-state value v_0 in 1 μs.

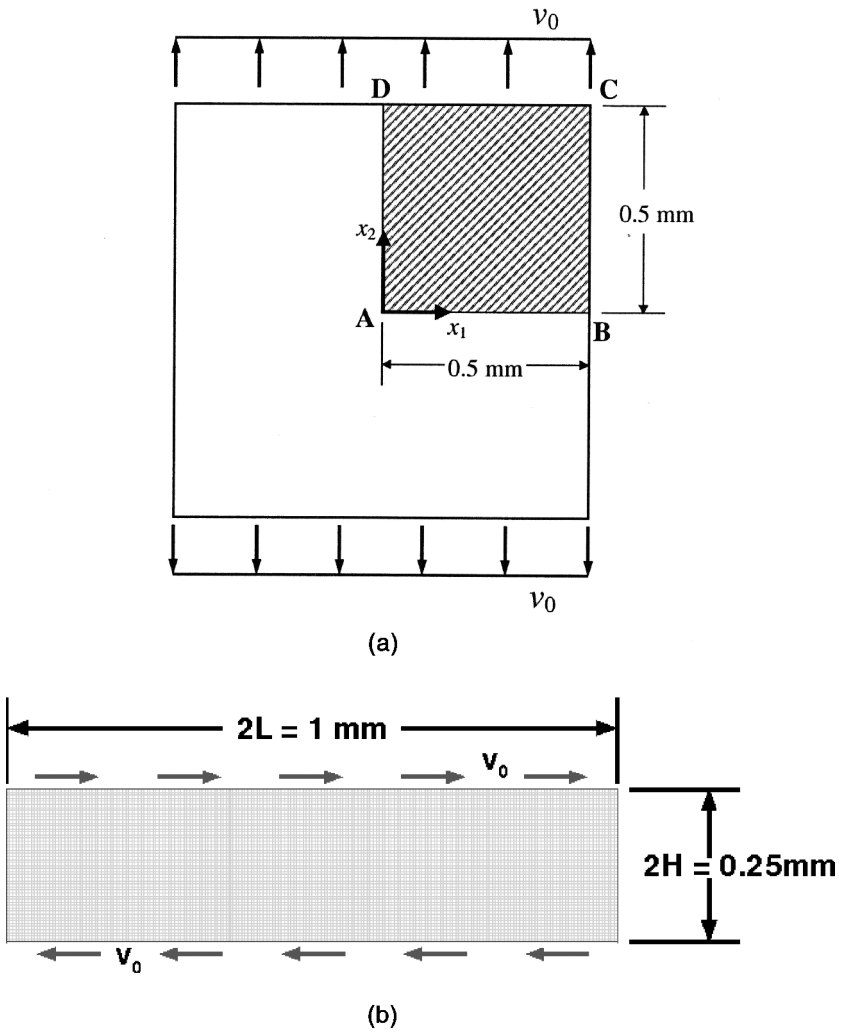

Figure 1 a) Schematic sketch of the plane strain tension problem, b) Schematic sketch for the plane strain simple shear problem, c) Effective stress vs. effective plastic strain curve for plane strain extensional deformations of tungsten and nickel-iron.

$$
\begin{aligned}
&T_{21} = T_{11} = 0,\ Q_1 = 0 \text{ on } X_1 = H \\
&T_{21} = 0,\ v_1 = 0,\ Q_1 = 0 \text{ on } X_1 = 0 \\
&T_{12} = 0,\ v_2 = 0,\ Q_2 = 0 \text{ on } X_2 = 0 \\
&T_{12} = 0,\ Q_2 = 0,\ v_2 = \begin{cases} v_0 t,\ 0 \le t \le 1\,\mu\text{s}, \\ v_0,\ t \ge 1\,\mu\text{s}, \end{cases} \quad \text{on } X_2 = H
\end{aligned}
\tag{17}
$$

Plane strain simple shearing deformations of a body of length $2L$ and height $2H$, as shown in Figure 1b, are also analyzed. Periodic boundary conditions are

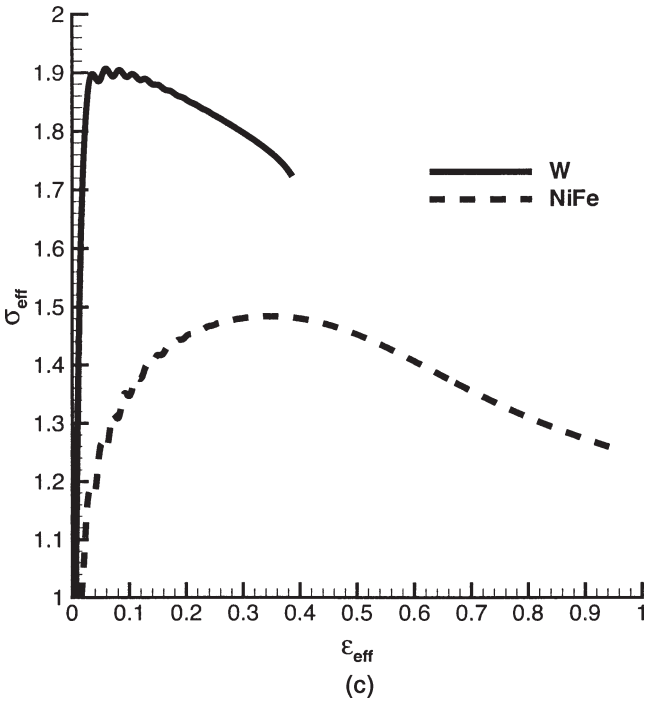

Figure 1 Continued.

applied on the surfaces $X_1 = \pm L$, which specify that the displacements and temperatures are equal at corresponding points and simulate an infinitely long specimen of height $2H$. The top and the bottom surfaces are taken to be smooth, thermally insulated and restrained from motion in the X_2-direction. Equal and opposite tangential velocity v_1 that increases linearly with time from zero to its final value v_0 in 1 μs is applied to the top and the bottom surfaces. Thus on $x_2 = \pm H$, we have

$$Q_2 = 0,\ v_2 = 0,\ v_1 = \begin{cases} \pm v_0 t, & 0 \le t \le 1\,\mu\text{s} \\ v_0, & t > 1\,\mu\text{s} \end{cases} \tag{18}$$

For $t > 1$ μs, the average strain-rate is v_0/H.

With the X_2-axis coincident with the centroidal axis of the cylinder and the X_1-axis in the radial direction, boundary conditions for the axisymmetric problem are the same as those for the plane strain problem listed above in Eq. (17).

Boundary conditions $(17)_{1-4}$, $(17)_{6-7}$, and $(17)_{9-11}$ are called natural and $(17)_5$, $(17)_8$, and $(17)_{12}$ essential.

The tungsten particulates are infinitely long circular cylinders for the plane strain and the simple shear problems, and circular rings for the axisymmetric problem.

Interface Conditions

It is assumed that, during the entire deformation process, the tungsten particulates are both mechanically and thermally perfectly bonded to the NiFe matrix. Thus

$$[\mathbf{u}] = \mathbf{0},\ [\theta] = 0,\ [T_{i\alpha}N_\alpha] = 0,\ [Q_\alpha N_\alpha] = 0 \text{ on } \Gamma \tag{19}$$

where $\mathbf{N}$ is an outward unit normal, in the reference configuration, to the interface Γ between a particulate and the matrix, $\mathbf{u}$ is the displacement of a point, and the square bracket indicates the jump of a quantity across the interface Γ between a particulate and the matrix.

Nondimensionalization of Variables

Let $\rho_R = \rho_0$, $\dot{\varepsilon}_R$, H, σ_0, and θ_R be the reference mass density, the reference strain rate, the reference length, the reference stress, and the reference temperature used to nondimensionalize quantities. Then in terms of nondimensional variables indicated by the same symbols as before, Eqs. (2) and (15) become

$$\alpha_I(1 - f_0)\dot{v}_i = T_{i\alpha,\alpha}, \quad i = 1,2,3\ \alpha = 1,2,3 \tag{20}$$

$$(1 - f_0)(\tau\ddot{\theta} + \dot{\theta}) = -\alpha_t\left(\left(1 - \frac{3}{2}f\right)\theta_{,\alpha}\right)_{,\alpha} + J\sigma_{ij}D^p_{ij}, \quad i,\ j = 1,2,3 \tag{21}$$

Here

$$\alpha_I = \frac{\rho_R\dot{\varepsilon}_R^2H^2}{\sigma_0},\ \alpha_t = \frac{\kappa}{\rho_R c H^2\dot{\varepsilon}_R},\ \theta_R = \frac{\sigma_0}{\rho_R c} \tag{22}$$

α_I and α_t are nondimensional measures of inertia and heat conduction effects, respectively. For a given material, inertia effects are directly proportional to the square of the reference strain rate and the square of the reference length. Heat conduction effects are inversely proportional to the reference strain rate and the square of the reference length. A possible choice for $2H$ is the length of a side of the square cross-section for the plane strain problem, the thickness of the block for the simple shearing problem, height of the cylinder for the axisymmetric problem, the particulate diameter, the smallest distance between any two particulates, the finite element size and that for $\dot{\varepsilon}_R$ is v_0/H. Indices i and j in Eq. (21) range over 1, 2, and 3 because σ_{33} and D^p_{33} need not vanish. In a plane strain problem, of course, $D_{33} = 0$. In a homogeneous material α_I influences the ASB initiation time and α_t the ASB width.

Semi-Discrete Formulation of the Problem

Eqs. (5), $(6)_2$, and (3) imply that the balance of moment of momentum (3) is identically satisfied. The present mass density can be computed from Eq. (1) if the deformation gradient and the current value of the porosity are known. Thus, the dependent variables to be solved for are $\mathbf{x}$, f, and θ and the independent variables are $\mathbf{X}$ and t. Eqs. (20) and (21) are second-order coupled nonlinear hyperbolic partial differential equations for $\mathbf{x}$ and θ. These cannot be written explicitly in terms of $\mathbf{x}$ and θ

since $\mathbf{T}$ is given by $(6)_2$ and $\dot{\boldsymbol{\sigma}}$ by (5), which involves $\mathbf{D}^p$ and θ. We solve the problem numerically by the finite element method (FEM).

We first introduce an auxiliary variable $\xi = \dot{\theta}$. Let $\psi_1, \psi_2, \ldots, \psi_n$ be the FE basis functions defined on Ω. We write

$$\begin{aligned} v_i &= \sum_{A=1}^{\text{nodes}} \psi_A(\mathbf{X})\tilde{v}_{Ai}(t), \;\; w_i = \sum_{A=1}^{\text{nodes}} \psi_A(\mathbf{X})c_{Ai}, \quad i = 1,2 \\ \theta &= \sum_{A=1}^{\text{nodes}} \psi_A(\mathbf{X})\tilde{\theta}_A(t), \;\; \xi = \sum_{A=1}^{\text{nodes}} \psi_A(\mathbf{X})\tilde{\xi}_A \end{aligned} \tag{23}$$

Here $\tilde{\mathbf{v}}$ is the vector of velocities of nodes, $\tilde{\boldsymbol{\theta}}$ the vector of nodal temperatures, $\tilde{\boldsymbol{\xi}}$ the vector of rate of change of temperature at the nodes, and c's are constants. Following the usual procedure, e.g., see [37], we get

$$\mathbf{M}\dot{\tilde{\mathbf{v}}} = -\mathbf{F}^{\text{int}}, \;\; \dot{\boldsymbol{\theta}} = \tilde{\boldsymbol{\xi}}, \;\; \tau\mathbf{H}\dot{\tilde{\boldsymbol{\xi}}} + \mathbf{H}\tilde{\boldsymbol{\xi}} = \mathbf{F}^{\theta} + \tilde{\mathbf{Q}} \tag{24}$$

where

$$\begin{aligned} M_{AB} &= \int_\Omega \alpha_I(1-f_0)\psi_A\psi_B d\Omega, \;\; F^{\text{int}}_{Ai} = \int_\Omega \psi_{A,\alpha}T_{i\alpha}d\Omega \\ H_{AB} &= \int_\Omega (1-f_0)\psi_A\psi_B d\Omega, \;\; F^{\theta}_{A} = \int_\Omega \alpha_t\left(1-\frac{3}{2}f\right)\theta_{,\alpha}\psi_{A,\alpha}d\Omega \\ Q_A &= \int_\Omega \psi_A J\,\text{tr}(\boldsymbol{\sigma}\mathbf{D}^p)d\Omega \end{aligned} \tag{25}$$

Note that the natural boundary conditions have been embedded in Eq. (24).

We solve Eq. (14) for $\dot{\varepsilon}^p_e$ in terms of σ_y, ε^p_e, and θ and derive its weak form in the same way as we derived Eq. (24) except that the divergence theorem is not used. Recall that $\dot{\varepsilon}^p_e > 0$ only when a material point is deforming plastically as signified by the satisfaction of Eq. $(8)_1$; otherwise $\dot{\varepsilon}^p_e = 0$. Weak forms of Eqs. (5), (14), and $\dot{\mathbf{x}} = \mathbf{v}(\mathbf{X}, t)$ are also derived. We thus get coupled nonlinear ordinary differential equations

$$\dot{\mathbf{d}} = \mathbf{F} \tag{26}$$

where $\mathbf{d}$ is the vector of unknowns and $\mathbf{F}$ is the force vector that depends upon time t and $\mathbf{d}(t)$. The 12 unknowns at a node are $\{x_1, x_2, v_1, v_2, \sigma_{11}, \sigma_{22}, \sigma_{12}, \sigma_{33}, f, \theta, \xi, \varepsilon^p_e\}$, and the dimension of vector $\mathbf{d}$ equals 12 times the number of nodes.

Values of Material Parameters

Values of thermophysical parameters for the W and the NiFe are listed in Table 1. Values assigned to other parameters given below in (27) are the same for the two constituents.

$$\begin{aligned} &\beta_1 = 1.5, \;\; \beta_2 = 1.0, \;\; f_2 = 0.04, \;\; s_2 = 0.1, \;\; \varepsilon_n = 0.5, \;\; \tau = 10^{-8}\text{s}, \;\; \theta_r = 273\,\text{K} \\ &f_c = 0.15, \;\; f_u = 2/3, \;\; f_f = 0.25 \end{aligned} \tag{27}$$

Table 1 Values of material parameters

Material	ρ (kg/m^3)	E (GPa)	ν	κ (W/m K)	c (J/(kg K))	α (10^{-6}/K)
Tungsten	19,300	400	0.29	160	138	5.3
NiFe	9,200	255	0.29	100	382	15

A (MPa)	B (MPa)	n	$\tilde{C}$	$\dot{\varepsilon}_0^p$ (1/s)	θ_m (K)	m
730	562	0.075	0.290	10^{-6}	1723	1.0
150	546	0.208	0.0838	10^{-6}	1225	1.0

Thus the acoustic impedances, $\sqrt{E\rho}$, of W and NiFe equal 87.86×10^6 and 48.44×10^6 kg/(m^{2}s) respectively and differ by a factor of 1.8. The bar wave speeds, $\sqrt{(E/\rho)}$, in W and NiFe are 4,552 and 5,265 m/s and differ by a factor of 0.86.

Figure 1c shows the effective stress versus the effective plastic strain curve for homogeneous W and NiFe bodies deformed in plane strain tension. It is clear that the yield stress for W is considerably higher than that for NiFe, the peak value of the effective stress in W is reached at a considerably lower value of the effective plastic strain than that in NiFe, and the thermal softening in W is significantly higher than that in NiFe.

Because of the random distribution of W particulates and the variation of the axial load with time t, the fraction of the axial load supported by W and NiFe at a horizontal surface $x_2 =$ constant varies with t. Once either one or both of these constituents begin to deform plastically, the speeds of incremental elastic waves in them will depend upon values of the tangent moduli. There are four nonzero components of the Cauchy stress tensor and the elastic strain tensor giving 16 elastic moduli for each material; these need not vanish simultaneously.

ASB Initiation Criterion in a Homogeneous Body

Batra and Rattazzi [38] studied the initiation and propagation of an ASB in a prenotched thick-walled steel tube and found that the choice of the ASB initiation criterion affected the predicted initiation time. They used four different criteria: (i) the effective plastic strain at a point equals 0.5, (ii) the effective plastic strain at a point equals 1.0, (iii) the effective stress at a point has dropped to 90% of its peak value at that point, and (iv) the effective stress at a point has dropped to 80% of its maximum value at that point; in each case the material point must be deforming plastically. Criteria (iii) and (iv) reflect Marchand and Duffy's [39] observation that the torque required to twist thin-walled tubes drops precipitously upon the initiation of an ASB. Batra and Kim [40] scrutinized ASBs in 12 materials deformed in simple shear and proposed criterion (iv), which we use in the present work to delineate if an ASB has initiated in a constituent. We note that the criterion (iv) was successfully used in [9] to ascertain the ASB initiation time in a functionally graded elastothermoviscoplastic body.

Length Scales

Besides the specimen size there are at least the following six length scales in the problem: (i) the viscous length $(\sqrt{E/\rho})/\dot{\varepsilon}_0^p$, (ii) the thermal length $\alpha_t H$, (iii) the particulate diameter, (iv) the smallest distance between any two particulates, (v) the finite element size and (vi) the inertial length $\alpha_t H$. The viscous length could also be defined as $\sqrt{(E/\rho)}H/v_0$. For the particulate composite each constituent has its own viscous, inertial and thermal lengths; these and other length scales for dipolar materials are given in Ref. [48].

For simple shearing deformations of a homogeneous and isotropic elastothermoviscoplastic material Batra [54] has scrutinized the effect of different material parameters and hence of length scales, and Batra and Kim [40] have obtained mesh independent results. Batra and Chen [34] have shown that the computed band width depends upon the specimen size. For dipolar materials Batra and Kim [49] found that the computed width of an ASB depends upon the material characteristic length introduced by the strain rate gradients and mesh-independent results can be easily computed; Batra and Liang [55] extended it to plane strain problems.

Time Scales

Time scales in the problem include $1/\dot{\varepsilon}_0^p$, H/v_0, $H\sqrt{\rho/E}$ and $1/\tau$. For a particulate composite each constituent has its own time scales. Furthermore, H can be replaced by either the particulate diameter or the smallest distance between any two particulates or the finite element size. Besides influencing the time step size in the numerical integration of Eqs. $(24)_1$ and $(24)_2$, it is not clear how they influence the ASB initiation time.

COMPUTATIONAL CONSIDERATIONS

Brief Description of the Computer Code

A computer code employing 4-node isoparametric quadrilateral elements has been developed. Integrals in Eq. (25) over each element are evaluated by using the 2×2 Gauss quadrature rule. Should a FE span two materials, values of the material parameters at the Gauss quadrature point are used. Batra [41] employed this procedure for analyzing finite static deformations of an inhomogeneous cylinder made of a Mooney–Rivlin material and showed that computed results matched well with the analytical solution. The coupled nonlinear ordinary differential Eq. (24) is modified to incorporate the essential boundary conditions in Eq. (17) and is then integrated with respect to time t by using the subroutine LSODE (Livermore Solver for Ordinary Differential Equations) that can be downloaded free from the internet. It adjusts adaptively the time step and the order of the integration scheme so as to compute a stable solution within the prescribed absolute and relative tolerances. Because of the large number of nodes in the FE mesh, the Adams-Moulton integration method obtained by setting $MF = 10$ in LSODE is employed.

Both the mechanical and the thermal problems are hyperbolic. Since the speed of the thermal wave is considerably smaller than that of the mechanical waves, the latter controls the size of the time step. Once deformations begin to localize even

at one point in the body, the time step drops significantly. This drop in the time step occurs at a lower value of the nominal strain for a particulate composite than that for a homogeneous body. It is because inhomogeneities in deformations introduced by numerous particulate/matrix interfaces induce localization, not necessarily simultaneously, of deformation at several discrete points in the body. Eventually the deformation localizes into a connected region that does not pass through all of the discrete points where the deformation had localized. For a 100×100 uniform FE mesh the CPU time is ~ 100 hours on a SGI single processor of an SGI Altix machine.

Verification of Code

The method of fictitious body forces (also called the method of manufactured solutions) is used to verify that the code correctly solves Eqs. (20) and (21). In this method, analytical expressions for the displacement and the temperature fields are presumed, and body forces and sources of internal energy (note that these had been set equal to zero in Eqs. (20) and (21)) are computed so as to satisfy the balance of linear momentum and the balance of internal energy. Also, initial and boundary conditions are derived from the assumed displacement and temperature fields. These are input into the code and the numerical solution is found. A good agreement between the computed and the analytical solutions verifies the code. This method was also used by Batra and Liang [42], e.g., see remarks following Eq. (30) of their paper.

For a shear band problem, computed results were also found to agree very well with those obtained by Batra and Lear [30] who employed a similar problem formulation but 3-node triangular elements. The code was used to study wave propagation in an inhomogeneous elastic bar [43]. The time histories of the computed wave speed and the axial stress at a point were found to agree well with the analytical solution of Chiu and Erdogan [44].

Effect of the FE Mesh

The finite element mesh used to analyze the problem is based on the numerical experiments described in Ref. [9] and the available computational resources. In [9] we used 40×40, 80×80, and 120×120 uniform FE meshes to delineate the initiation of an ASB in an inhomogeneous $5\,\text{mm} \times 5\,\text{mm}$ body. The material properties varied continuously in the radial direction. The ASB initiation times with the three meshes were found to be 65.9, 64.8, and 64.5 μs respectively, and the corresponding CPU times were 1133, 6908, and 29242 s. Thus a 40×40 uniform FE mesh can predict well the ASB initiation time. Similar results were found in [30] for a homogeneous body.

RESULTS

Plane Strain Tensile Deformations

Effect of particulate size The $0.5\,\text{mm} \times 0.5\,\text{mm}$ region is divided into 100×100 uniform 4-node quadrilateral elements. Keeping the volume fraction of W particulates fixed at 50%, random distributions of 40, 50, 60, and 75 μm diameter

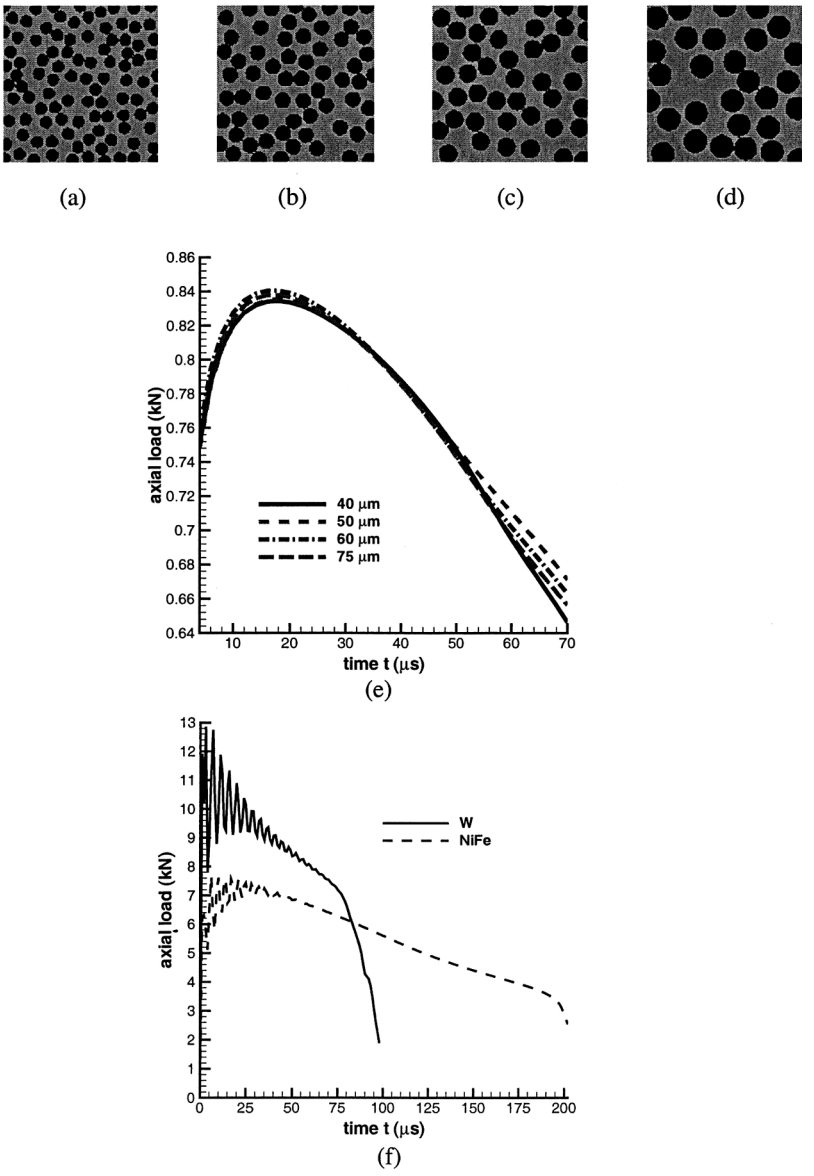

Figure 2 W (particulate)/NiFe (matrix) with particulate diameter (a) 40 μm; (b) 50 μm; (c) 60 μm; (d) 75 μm; (e) axial load versus time for (a)–(d); and (f) axial load vs. time for homogeneous bodies comprised of W and NiFe.

particulates, as shown in Figures 2a–d, are considered. These particulate diameters are typical of those employed by Dick et al. [15] in their experiments on WHAs. The prescribed velocity on the top surface increases linearly from 0 to 0.25 m/s in 1 μs and then stays steady. Thus for $t > 1$ μs the nominal axial strain rate induced in the body is 5000/s. Time histories of the axial load computed from the axial stress

at nodes on the top surface are plotted in Figure 2e. As for a homogeneous body, with the continuous application of the axial velocity, the axial load first increases, reaches a plateau and then drops rapidly; the results for a pure W and a NiFe block are given in Figure 2f. Whereas for $0 < t \leq 50\,\mu s$ the time-history of the axial load exhibits oscillations for a homogeneous body, it varies rather smoothly for the particulate composite. Even though the peak load for a particulate composite varies slightly with the particulate size, it occurs at an axial strain of ~ 0.08 for the four particulate sizes considered. For a homogeneous body having zero initial porosity, the load drops rapidly at axial strains of ~ 0.386 and ~ 0.944 for W and NiFe respectively. With an initial nonuniform porosity distribution having a maximum value of 2.5% at the specimen centroid the rapid load drop initiated at an axial strain of ~ 0.137 in the otherwise homogeneous body made of W; see [9]. Thus the presence of initial defects strongly influences the time when the load begins to drop and an ASB initiates and eventually develops. The mismatch between the properties of the particulates and the matrix introduces a much stronger defect than that introduced by the initial nonuniform distribution of porosity. The results plotted in Figure 2e suggest that the particulate size affects neither the axial strain when the peak in the axial load occurs nor the rate of drop of the axial load. Also the load drops rather gradually in a particulate composite than in the homogeneous body. Neither in the particulate composites nor in the two homogeneous materials does an ASB initiate when the axial load attains its peak value. The computed axial load incorporates the softening induced due to the heating of the specimen, porosity evolution and the decrease in the area of cross-section, i.e., due to damage, geometric and thermal effects.

For the simple shearing deformations of a homogeneous body Molinari and Clifton [45] have given a relation between the defect size and the time when the deformation localizes. Batra and Kim [40] have studied numerically the influence of the defect size on the time of initiation of an ASB and also on the eventual bandwidth. These investigations reveal that the time of initiation of the localization of deformation decreases exponentially with an increase in the defect size. However, the equivalence relation among different defect types—porosity, rigid inclusion, variation in dimensions of the specimen (or a geometric defect), boundary conditions such as frictional forces, and/or thermal energy input through the boundaries, and interfaces between distinct materials—has not been scrutinized.

In order to delineate the initiation and development of an ASB in a particulate composite, we have exhibited in Figure 3 fringe plots of the effective plastic strain at five different times for the case of 40 μm diameter particulates. With an increase in the average axial strain the softer NiFe matrix undergoes more intense plastic deformations as compared to those of W particulates. Figure 3a exhibits several narrow regions of large plastic deformation at $t = 30\,\mu s$. During the subsequent $10\,\mu s$, the effective plastic strain has grown in many of these regions. However, it is hard to delineate where an ASB will eventually develop. There seem to be at least two regions of large plastic deformation in Figures 3c and 3d. Even at an average axial strain of 0.35 there are many regions where the effective plastic strain is nearly 100%. We now attempt to delineate which ones, if any, of these regions correspond to ASBs.

Figure 4 shows the axial stress σ_{yy} and the effective plastic strain as a function of time in the 40 μm particulate diameter composite at two arbitrarily chosen points:

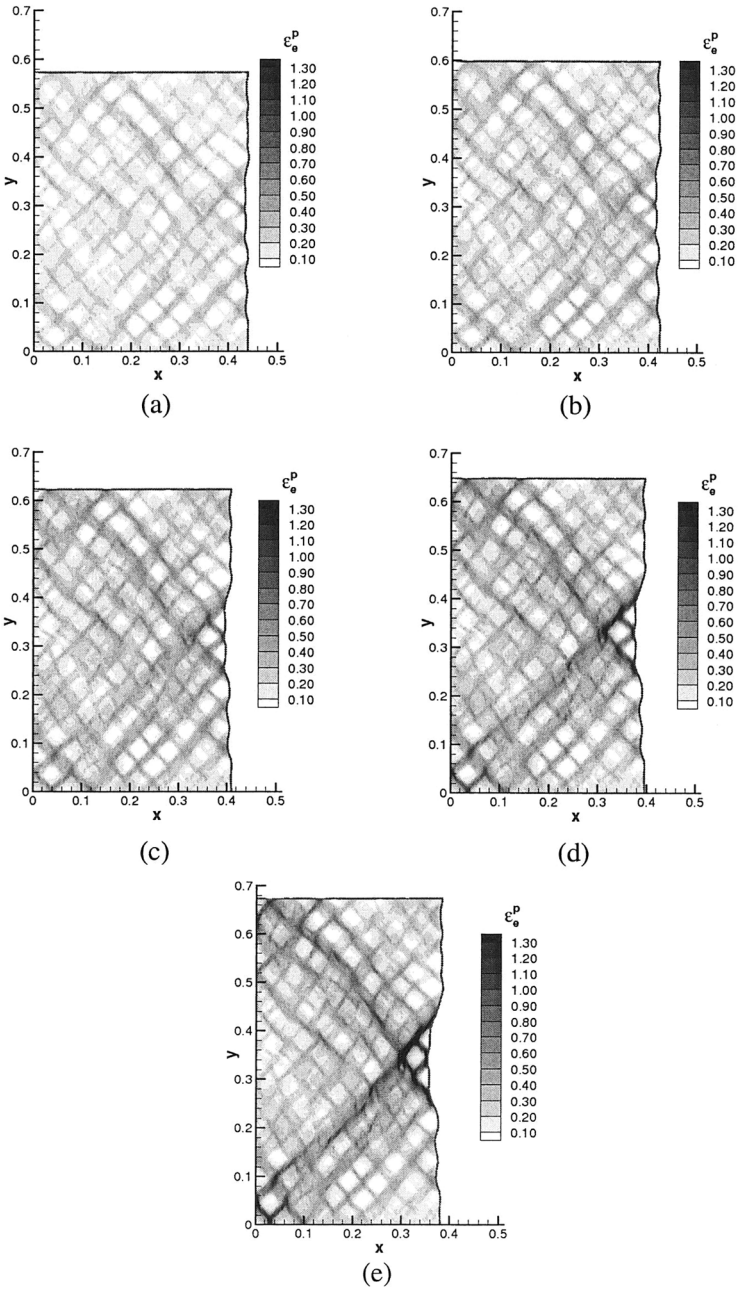

Figure 3 Contours of effective plastic strain with W particulates of diameter 40 μm at (a) 30 μs, (b) 40 μs, (c) 50 μs, (d) 60 μs, and (e) 70 μs.

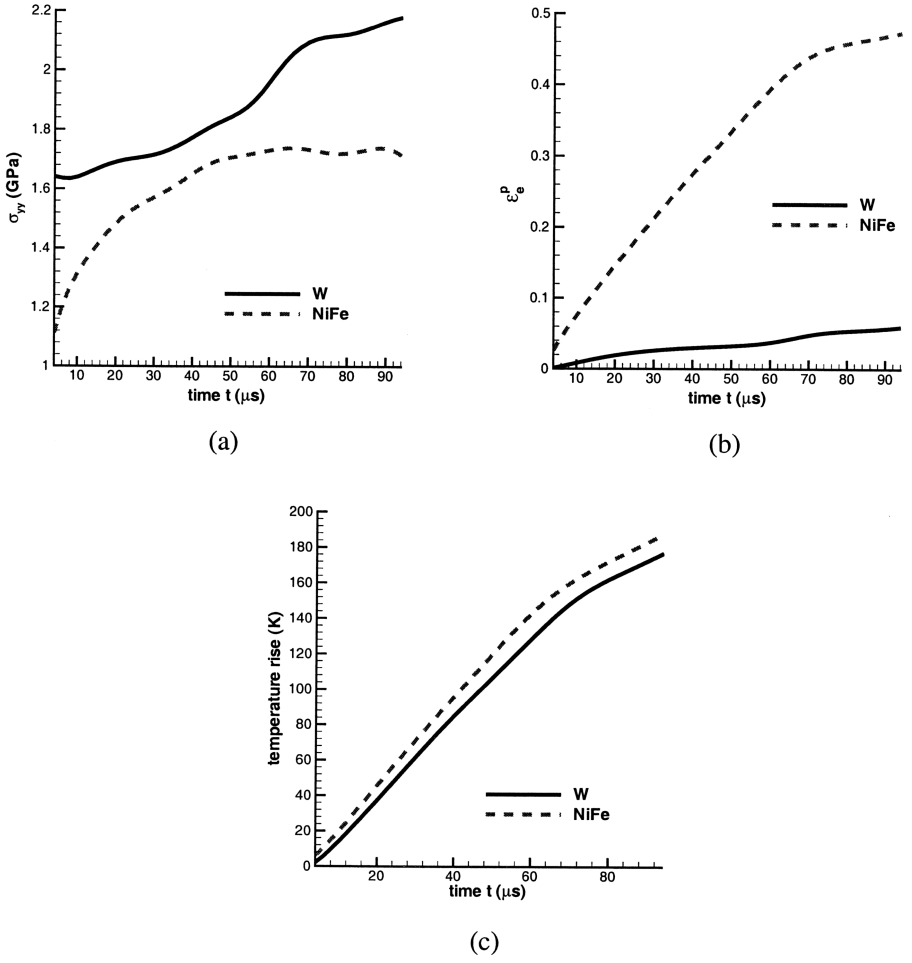

Figure 4 Time histories of (a) axial stress, (b) effective plastic strain, and (c) temperature rise at two nearby points, one inside a particulate and the other in the matrix for the 40 μm particulate diameter composite.

a point inside W initially located at $(X_1, X_2) = (0.06, 0.4)$ and a nearby point located inside the NiFe matrix initially at $(0.085, 0.4)$. At any time the effective plastic strain is much higher in the NiFe matrix than that in the W particulate and the axial stress is higher in the W than that in the NiFe. Because of the assumption of perfect bonding between the two materials, displacements, surface tractions, temperature, and the normal component of the heat flux at common interfaces between them are continuous. Even though the quasistatic yield stress of W is nearly three times that of NiFe, for $t > 10\,\mu s$ the effective stress in W is only a little higher than that in NiFe because of the large differences in their strain- and strain-rate hardening characteristics. However, results plotted in Figure 4b reveal that, at any time t, the effective plastic strain in W is less than one-third that in NiFe. Since the heat capacity ρc of W is approximately 30% higher than that of NiFe, the temperature rise in W is slightly

less than that in NiFe; this is depicted in Figure 4c. The two materials are softened thermally at different rates due to differences in their temperatures and thermal softening parameters. Thus effective plastic strain rates are different in the two materials. Results plotted in Figure 4b suggest that for $t \leq 70\,\mu s$ the effective plastic strain rate at the point in the NiFe matrix is considerably more than that in the W particulate. At $t \approx 70\,\mu s$ or the average axial strain of about 0.35, the effective plastic strain rates at both points decrease noticeably; the change being more noticeable for the point in the NiFe matrix than that for the point in the W particulate.

For $t = 80.1\,\mu s$ and $t = 90.1\,\mu s$, Figure 5 depicts points where the ASB initiation criterion for a homogeneous material described previously has been satisfied and also contours of the effective plastic strain. Attempts to find the time sequence in which ASBs initiated at these points failed since the state of deformation at a material point satisfied the ASB initiation criterion at $t = t_1$ but did not do so at $t = t_2 > t_1$. Points where the ASB criterion has been satisfied at either one of these two times do not lie on a continuous curve and hence do not form a discernible ASB, despite the high levels of deformation exhibited in the corresponding contours of the effective plastic strain. It is thus clear that the ASB initiation criterion in a particulate composite is different from that in a body with either uniform or continuous variation of material properties.

After a close scrutiny of the spatial and the temporal variations of different measures of deformation, it was found that at late stages of deformation, the spatial variations of the axial velocity and the rate of change of temperature are similar. At points where the axial velocity varies sharply, the rate of increase of temperature is also very high. In locally adiabatic deformations, the rate of increase of temperature equals the energy dissipation rate/mass divided by the specific heat. In general, the heat conduction, the energy dissipation rate and the heat capacity influence the rate of temperature rise at a point.

For a particulate composite with 50% volume fraction of $40\,\mu m$ diameter W particulates in NiFe matrix, Figure 6 evinces contour plots of the axial velocity and the rate of increase of temperature at an axial strain of 35%, or equivalently $t = 70\,\mu s$. It is clear that the axial velocity varies sharply across regions where the rate of increase of temperature is also extremely large. These results suggest that at an average axial strain of ~ 0.35 or at $\sim 70\,\mu s$ the deformation has localized into two regions across which the axial velocity and the rate of change of temperature vary sharply. We note that during the simple shearing and the plane strain deformations of a homogeneous material the tangential velocity has a steep gradient across an ASB. Thus the development of a narrow region across which the tangential velocity varies sharply is synonymous with the formation of an ASB in monolithic materials, materials with continuously varying thermo-mechanical parameters and particulate composites. However, this can only be discerned by post-processing results of the numerical solution.

Equivalent homogenized body One would like to replace the particulate composite with a homogeneous material whose effective properties are obtained by either analyzing deformations of a representative volume element (RVE) or by the rule of mixtures. Love and Batra [46] found that, except for the strain-rate hardening coefficient $\tilde{C}$, the two methods give esstentially the same values of various

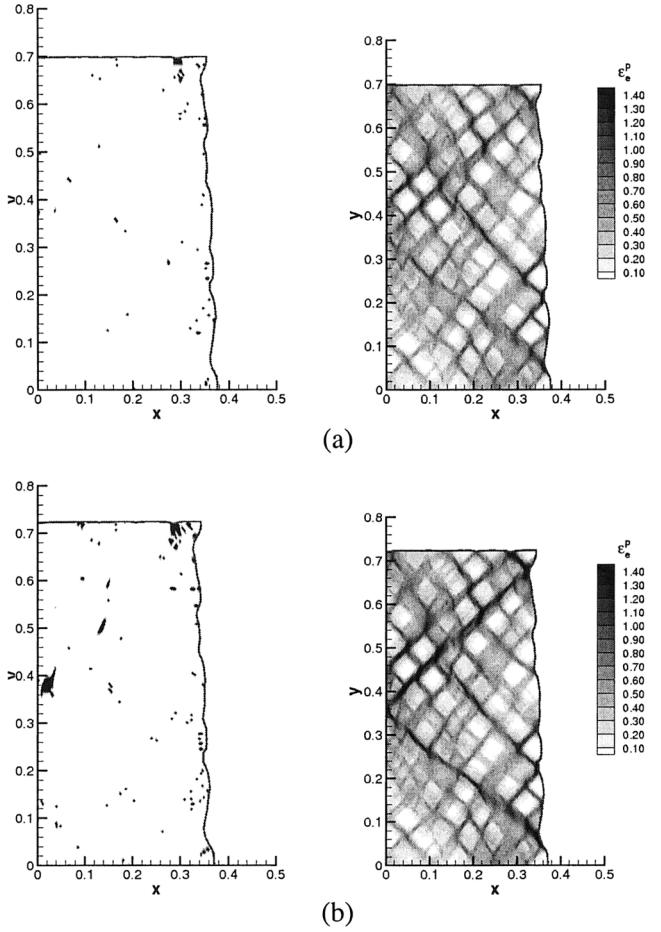

Figure 5 Points satisfying the ASB initiation criterion and contours of effective plastic strain in a W/NiFe particulate composite with 50 μm diameter tungsten particulates at (a) 80.1 μs and (b) 90.1 μs.

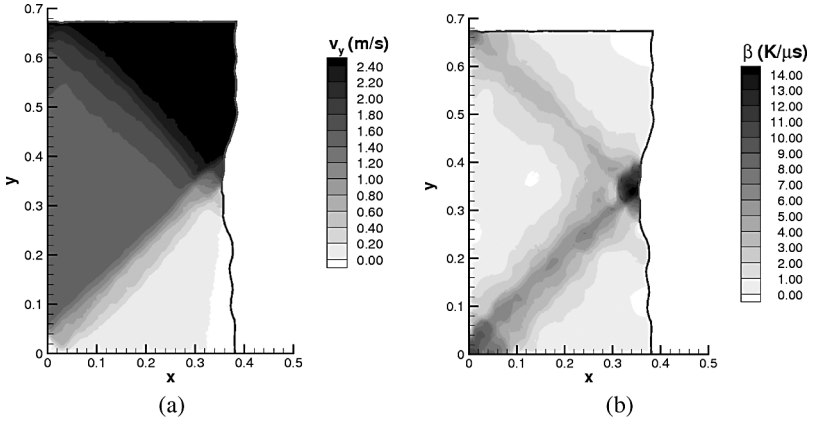

Figure 6 Contours of (a) axial velocity and (b) rate of increase of temperature, β, in a particulate composite with 40 μm diameter particulates at an axial strain of 35%.

material parameters that are independent of the particulate size. Here we have employed values of the thermomechanical parameters found by analyzing deformations of a RVE [46].

The particulate composite possesses many particulate/matrix interfaces that act as local defects. We propose to simulate the cumulative effect of these defects in the homogeneous body with an initial porosity distribution $f_0(\mathbf{X})$ given by

$$f_0(\mathbf{X}) = \begin{cases} f_{ce}(1 - \frac{r}{H}), & 0 \le r \le H \\ 0, & r \ge H \end{cases} \tag{28}$$

Here $r = \sqrt{X_\alpha X_\alpha}$ is the distance from the centroid in the reference configuration and $H = 0.5\,\text{mm}$ is the height of the specimen. The porosity f_{ce} at the centroid is varied such that the rates of increase of temperature at points where an ASB develops in the particulate composite and in the homogeneous material are similar. Figure 7 shows

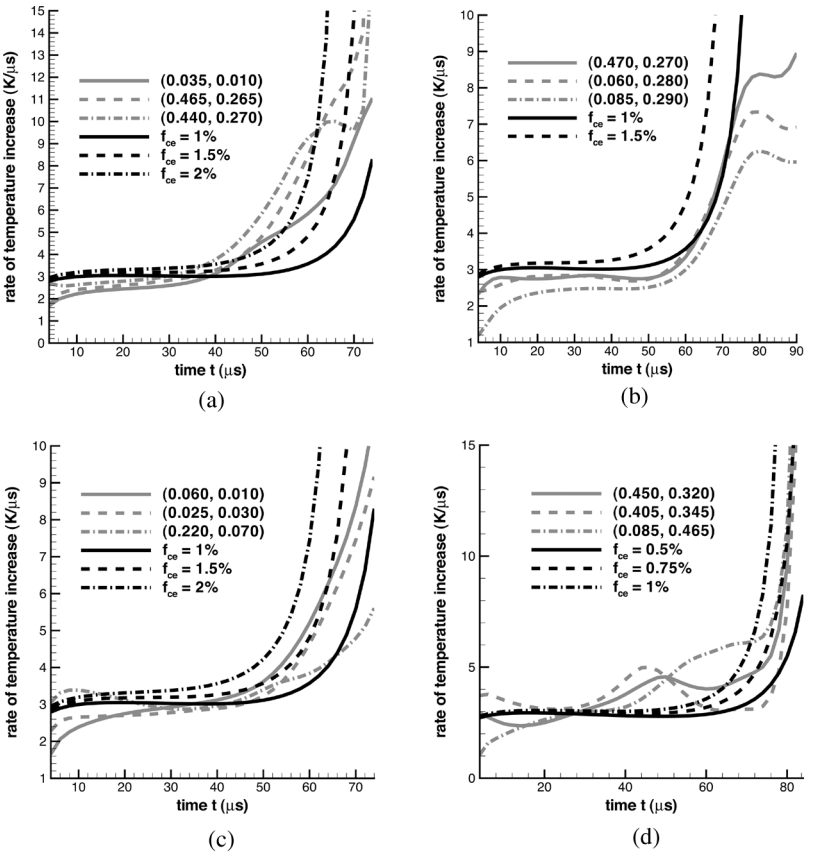

Figure 7 Rate of increase in temperature at a point inside the ASB in 50/50 W/NiFe particulate composites with particulate diameters of (a) 40 μm, (b) 50 μm, (c) 60 μm, and (d) 75 μm, as well as the rate of increase of temperature at the centroid of equivalent homogeneous bodies with nonuniform initial porosity; coordinates denote the position of the point in the particulate composite in the reference configuration.

the time histories of the rate of increase of temperature for three nodes inside the ASB in each of the four particulate composites and the rate of increase of temperature at the centroid of an equivalent homogeneous body for different values of f_{ce}. The nodes in the particulate composites were selected in local regions of intense plastic deformation that also saw a large rate of change of temperature; their coordinates in the reference configuration are listed in the figure.

Note that the rate of increase of temperature for the homogeneous body increases monotonically with time; that for the particulate composites shows some fluctuations at different nodes that have been smoothened out in the plots. Furthermore, at any time t several nodes in a particulate composite exhibit heating at similar rates. This behavior is not seen in the homogeneous body, where the centroid is heated more rapidly than other points in the body. These severely heated points in a particulate composite may be disconnected. In a homogeneous body, the ASB originates at the centroid and propagates at 45° in the present configuration. In a particulate composite the point of initiation of an ASB can be discerned by post-processing the numerical solution. ASB formation and propagation in the particulate composite is more complex. The ASB initiation criterion for a homogeneous body may have been satisfied either simultaneously or sequentially at several points. However, the eventual ASB may not pass through all of these points.

We postulate that an ASB initiates at a point when the slope of the $\dot{\theta}$ vs. t curve for the point suddenly increases by an order of magnitude. Note that the slope of $\dot{\theta}$ vs. t curve equals the curvature of θ vs. t curve. The ASB initiation times for the four particulate diameters computed according to this criterion are listed in Table 2. Whereas for the 40 and the 60 μm diameter particulates the ASB initiation times at the three points vary noticeably those for the 50 and the 75 μm diameter particulates are relatively close to each other. These variations in the ASB initiation times can not be attributed to the constituent of the three points. For each particulate diameter considered, an ASB passes through NiFe and W.

For the equivalent homogenized body the ASB initiation times for the three values of the initial porosity at the specimen centroid are compared with that for the particulate composite in Table 3. Whereas we can find f_{ce} so that an ASB initiates in a particulate composite and in the equivalent homogenized body at about the same time, the orientations and the centers of the ASB in the two bodies will generally be quite different.

Dai et al. [47] studied ASB initiation in a composite body comprised of SiC particles immersed in aluminum. The specimens were twisted in a split Hopkinson bar with presumably the same torsional impulse. They found that ASBs formed

Table 2 Effect of particulate diameter on the ASB initiation times

	Material, and ASB initiation time (μs)			
Particulate diameter (μm)	Point 1	Point 2	Point 3	Average
40	NiFe, 66	W, 50	W, 44	53
50	W, 58	W, 56	NiFe, 60	58
60	W, 52	W, 54	W, 64	56.7
75	W, 74	NiFe, 76	W, 76	75.3

Table 3 Effect of initial porosity in the homogenized body on the ASB initiation times

Particulate composite				
Particulate diameter μm	ASB initiation time (μs)	$(f_{ce},\ t_{SB})$ in the equivalent homogenized body. t_{SB} is in μs.		
40	53	(0.01, 64)	(0.015, 54)	(0.02, 48)
50	58	(0.01, 64)	(0.015, 54)	—
60	56.7	(0.01, 64)	(0.015, 54)	(0.02, 48)
75	75.3	(0.005, 74)	(0.0075, 68)	(0.01, 64)

more readily as the particulate size was reduced, and the maximum shear strain induced in particulate composites increased as the particulate diameter was reduced. They explained this by conjecturing that strain gradients increase with a decrease in the particulate diameter and they provide a driving force for the formation of ASBs. Batra [48] and Batra and Kim [49] showed that the consideration of strain-rate gradients and the corresponding higher-order stresses delays the initiation of an ASB. In order to see how strain gradients depend upon the particulate size, we have plotted in Figure 8 the spatial variation on the line $x_2 = 0.4$ mm of the mass density and the effective plastic strain for the four particulate sizes considered when the average axial strain in each composite equals 0.25. The line $x_2 = 0.4$ mm and the time $t = 50$ μs are arbitrarily chosen. As expected sharp gradients in the effective plastic strain occur at points adjacent to the particulate/matrix interface. For each particulate composite there are sharp spatial gradients in the effective plastic strain.

The effective plastic strain in W is considerably less than that in NiFe; the location of a W particulate is identified from the plot of the mass density. The peak magnitude of the effective plastic strain gradient and where it occurs are different for the four particulate composites. It is reasonable to expect that the maximum magnitude of the strain gradient and its location vary with time. At $t = 50$ μs the maximum strain gradient on the line $x_2 = 0.4$ mm equals $\sim 1700/\text{m}$. One difference between Dai et al.'s and the present work is that SiC particulates in the aluminum matrix undergo very little deformation. However, W particulates within an ASB are severely deformed. Another difference is that in Dai et al.'s work [47] the volume fraction of 3.5, 10, and 20 μm SiC particles equalled 15%, and in the present work the volume fraction of 40, 50, 60, and 75 μm diameter W particulates is 50%. In spite of these differences ASB initiation times listed in Table 2 agree qualitatively with Dai et al.'s [47] experimental observations. We should add that Dai et al. identify an ASB with a narrow region of intense plastic deformation. Furthermore, they assume that an ASB initiates at a point when the shear stress there peaks. However, as shown herein an ASB usually initiates much later; also see [30,40,34].

Batra and Kim [50] and Kwon and Batra [51] explored the initiation of ASBs in simple and dipolar (strain-rate gradient dependent) materials deformed in simple shear and introduced a sinusoidal defect with multiple peaks of the same amplitude. These can be viewed as inhomogeneities introduced by particulate/matrix interfaces. They found stark differences in the ASB development in simple and dipolar materials. Batra and Kwon [52] studied the initiation and the development of an ASB during simple shearing deformations of a bimetallic body with the upper half made of one

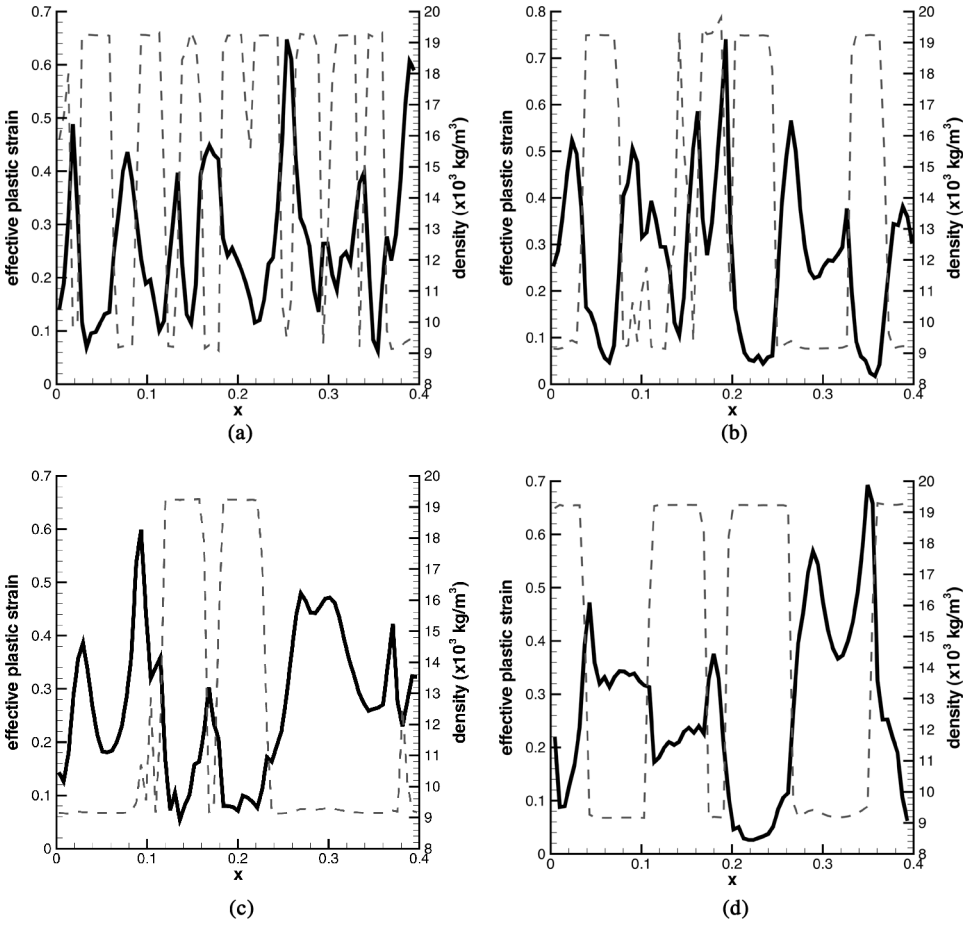

Figure 8 At an average axial strain of 0.25, variation of the mass density (dashed line) and the effective plastic strain (thick line) along $x_2 = 0.4$ mm for particulate composites with particulate diameters of (a) 40 μm, (b) 50 μm, (c) 60 μm, and (d) 75 μm.

material and the lower half comprised of a different material. They found that the thermal softening characteristics of the two constituents significantly influenced the location of the ASB and it formed completely in the constituent exhibiting higher thermal softening. When one of the constituents has very low thermal conductivity relative to the other one, plastic strain rates in it are higher at points equidistant from the centerline of the specimen.

Effect of particulate arrangement In order to assess the effect of the particulate arrangement, we have plotted in Figure 9 fringes of the axial velocity and the rate of temperature increase for three different random distributions of 50 μm diameter particulates. It is clear that the particulate placements strongly influence when and where an ASB initiates. For example in Figure 9a, an ASB seems to have originated from a point on the vertical centoidal axis and propagated at $\pm 45°$, but in

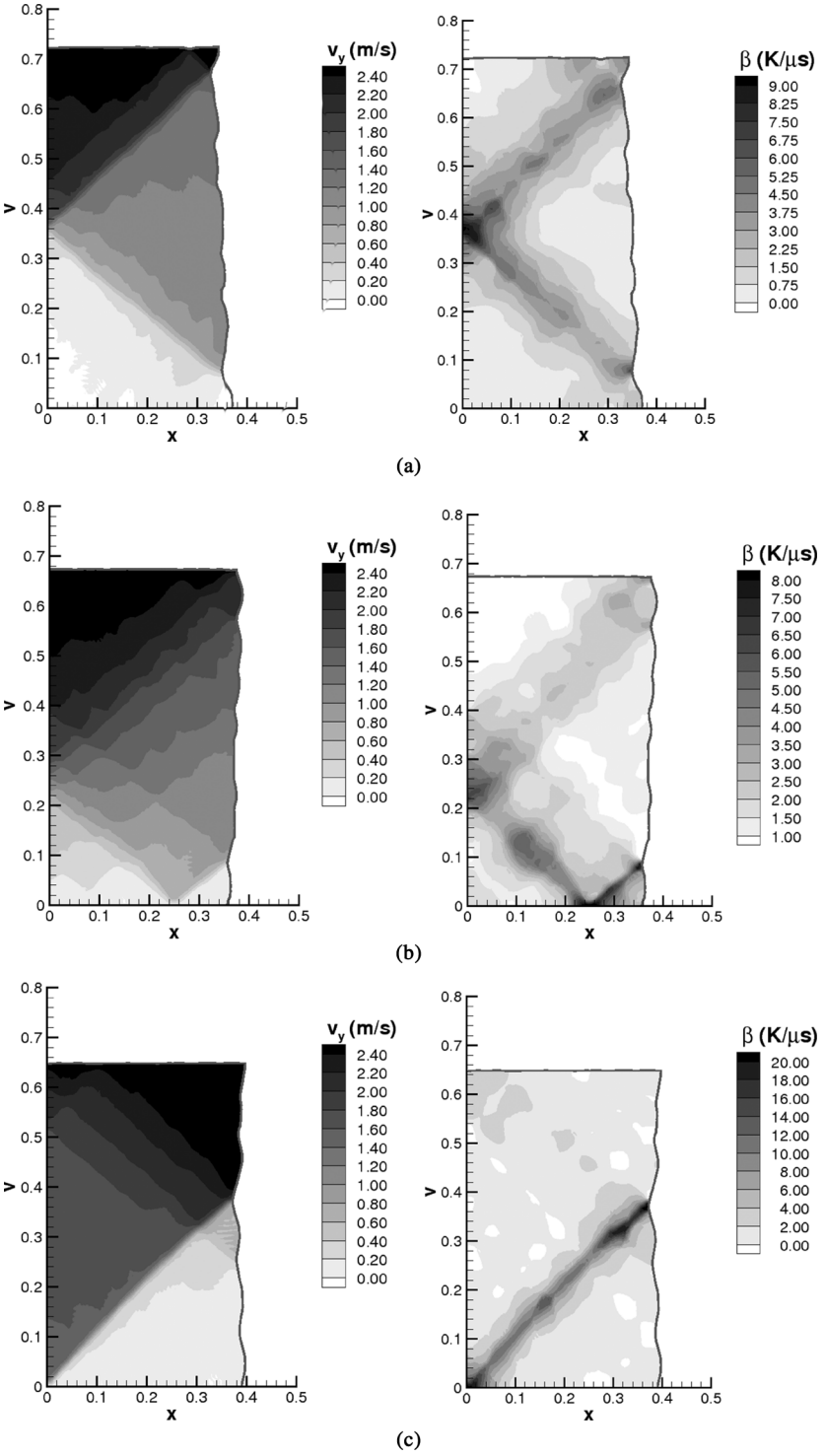

Figure 9 Contours of the axial velocity and the rate of temperature increase β, for three different random arrangements of 50 μm diameter particulates: (a) arrangement 1 at 90 μs, (b) arrangement 2 at 70 μs, and (c) arrangement 3 at 60 μs.

Figure 9c, the origin of the ASB is at a point on the free surface and it propagated only towards the centroid of the cross-section. Furthermore, the times of initiation equal ~ 90 μs and 60 μs for particulate distributions of Figures 9a and 9c, respectively. For the particulate distribution of Figure 9b, there is no narrow region across which the axial velocity increases sharply. The plots of the rate of temperature increase depicted in Figure 9 support the aforementioned remarks for the three particulate arrangements.

The variation of the mass density and the effective plastic strain on the line $x_2 = 0.4$ mm is exhibited in Figure 10. It is apparent that strain gradients are higher for the particulate arrangement of Figure 10b than those for the other two arrangements analyzed. The time histories of the rate of temperature rise, at three material points, evinced in Figure 11 suggest that an ASB initiates at $t \approx 60$ μs. The ASB initiation times computed according to the criterion hypothesized above and the material of the point are listed in Table 4. There is less variation in the ASB initiation time than in the contour plots of the axial velocity and the rate of temperature increase. An initial affine porosity variation with approximately 1.25% porosity at the specimen centroid in the equivalent homogenized body will result in the ASB initiating at $t \approx 60$ μs.

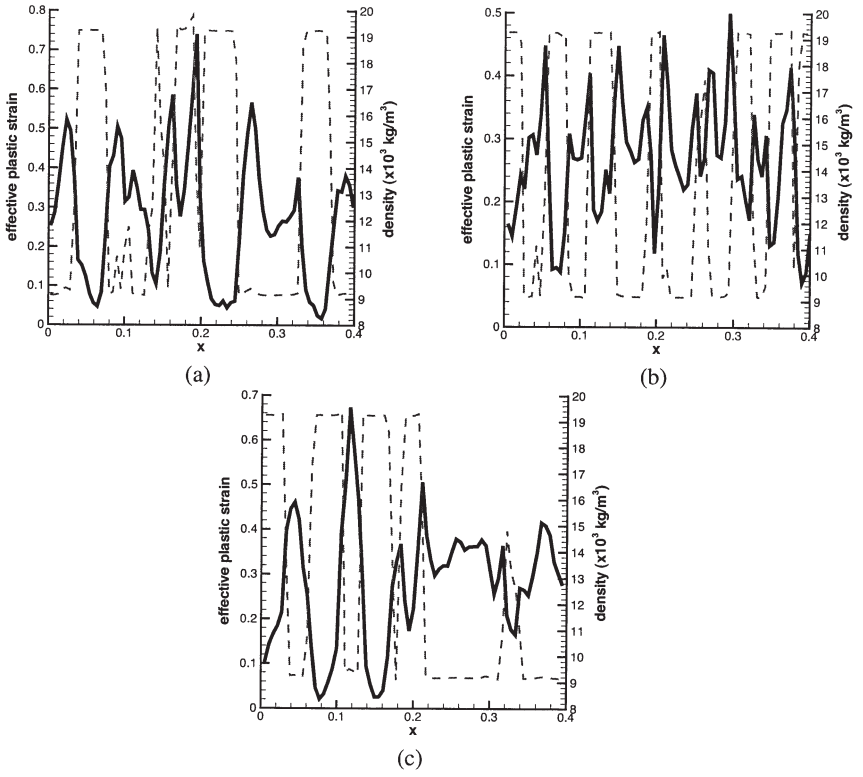

Figure 10 At an average axial strain of 0.25, variation of the mass density (dashed line) and the effective plastic strain (solid line) along $x_2 = 0.4$ mm for particulate composites with randomly distributed 50 μm diameter particulates: (a) arrangement 1, (b) arrangement 2, and (c) arrangement 3.

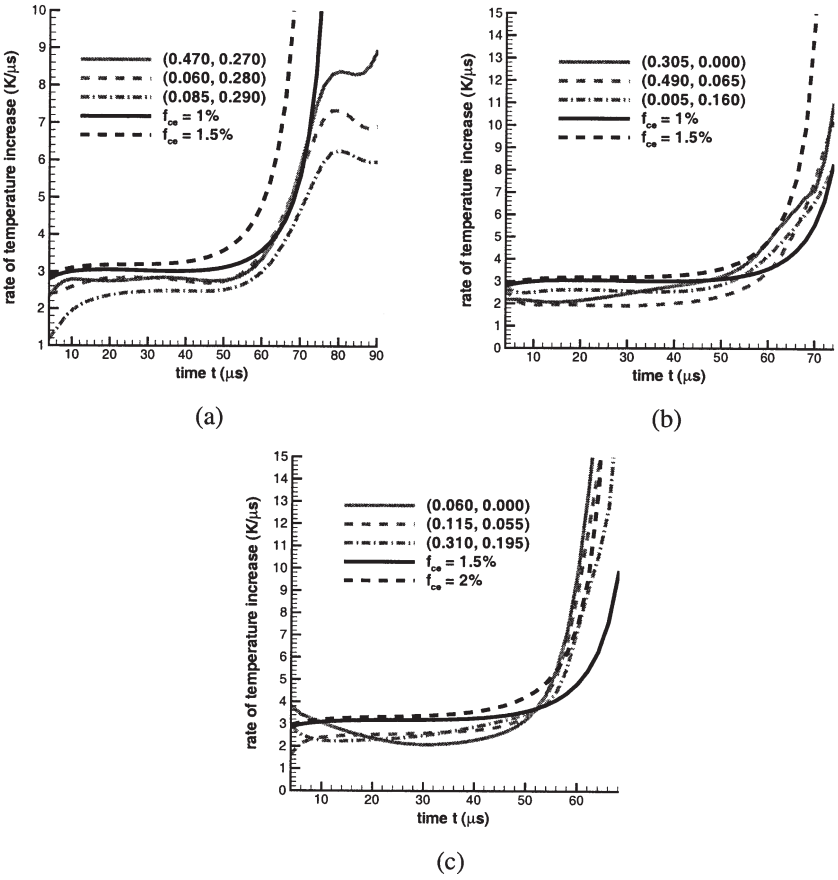

Figure 11 Rate of increase in temperature at a point inside the ASB in 50/50 W/NiFe particulate composites with particulate diameters of 50 μm for (a) arrangement 1, (b) arrangement 2, and (c) arrangement 3, as well as the rate of increase of temperature at the centroid of equivalent homogeneous bodies with non-uniform initial porosity; coordinates denote the position of the point in the particulate composite in the reference configuration.

We note that the time histories of the axial load plotted in Figure 2e indicate that the drop in the axial load to 80% of its peak value occurs at $64\,\mu s \leq t \leq 68\,\mu s$ for the four particulate diameters. Whether or not it can be used as a criterion for the ASB initiation remains to be investigated.

Table 4 Effect of particulate arrangement on ASB initiation time

	Material, and ASB initiation time (μs)			
Particulate arrangement	Point 1	Point 2	Point 3	Average
1	W, 58	W, 56	NiFe, 60	58
2	NiFe, 58	NiFe, 60	NiFe, 56	58
3	W, 52	NiFe, 52	NiFe, 56	53.3

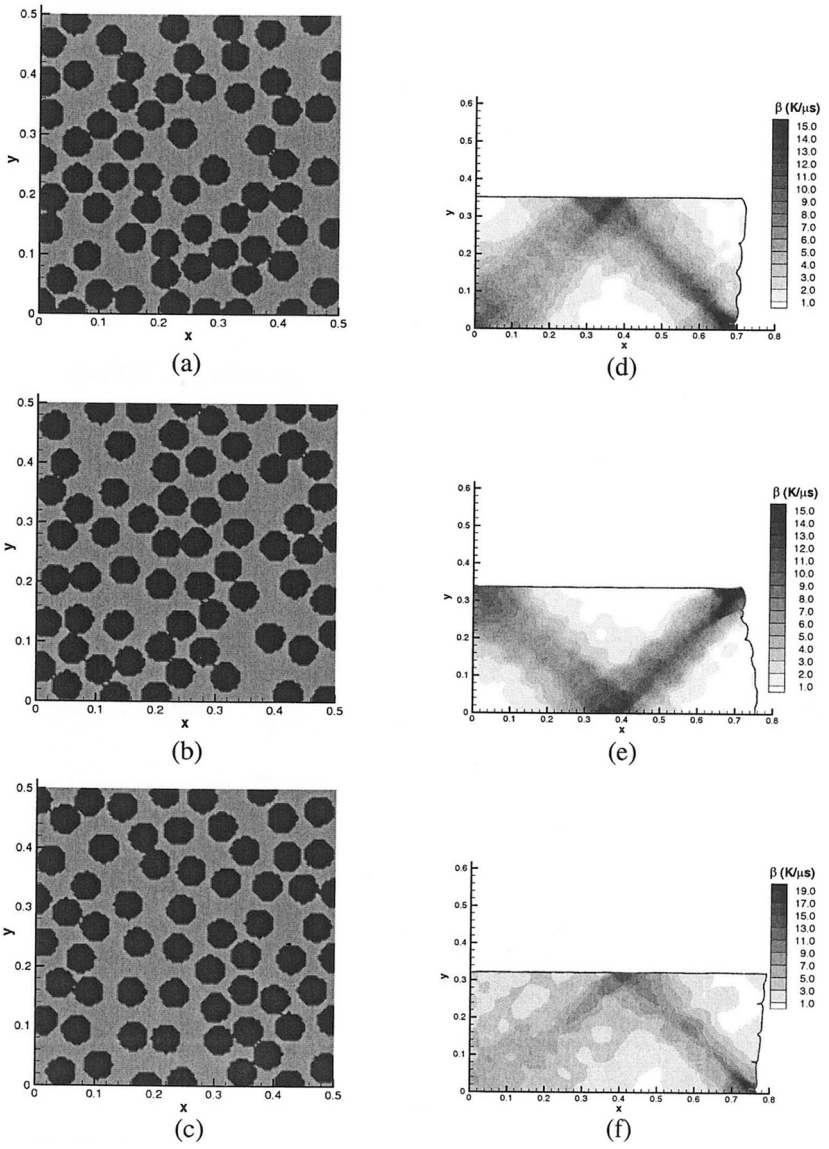

Figure 12 For the plane strain compression of 50/50 W/NiFe particulate composites, (a)–(c) the three random particulate arrangements, and (d)–(f) fringe plots of the rate of temperature rise, β at time $t = 66.6\,\mu s$.

Plane Strain Compressive Deformations

The three randomly assigned particulate arrangements of 50/50 W/NiFe composite for studying plane strain compressive deformations are evinced in Figure 12. Frictional forces between the loading device and the specimen are neglected. Because of the increase in the width of the specimen while it is being compressed there is a geometric hardening effect. Also the hydrostatic pressure is likely to be compressive,

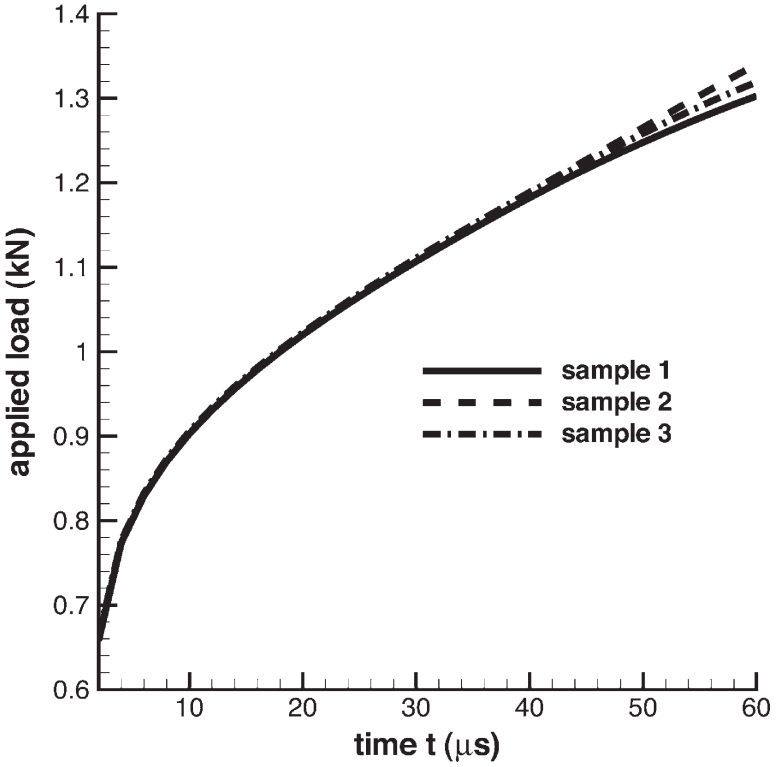

Figure 13 Time history of the axial load for plane strain compression of three particulate arrangements in the 50/50 W/NiFe 40 μm diameter particulate composite.

implying that no new voids will nucleate. Thus unless thermal softening exceeds hardening due to strain, strain-rate, and geometric effects the axial load required to deform the specimen will increase monotonically. The time history of the axial load depicted in Figure 13 reveals that hardening effects dominate. However, the deformation does localize as evidenced by the fringe plots of the rate of temperature rise in Figure 12d–f. For each particulate arrangement the shape of the intensely deforming region in the X_1X_2-plane is like V or Λ. As for the plane strain tensile deformations one can find the shape, the time of initiation, and the center of the ASB by post processing the computed solution.

For the particulate arrangement of Figure 12b we estimated the center line of the ASB from the fringe plots of the rate of temperature rise and drew a line perpendicular to it; this line across the ASB is depicted in Figure 14a. The computed axial velocity, the rate of temperature rise, and the effective plastic strain at numerous points on a line perpendicular to the centerline of the ASB are exhibited in Figure 14b-e. The abcissa equals the distance of a point from (0.7 mm, 0). It is clear that the variation of the effective plastic strain across an ASB is quite oscillatory and cannot be used to determine the ASB width. However, the rate of temperature rise varies smoothly across an ASB and can be used to ascertain its width. Both the temperature rise and the axial velocity also vary smoothly across an ASB.

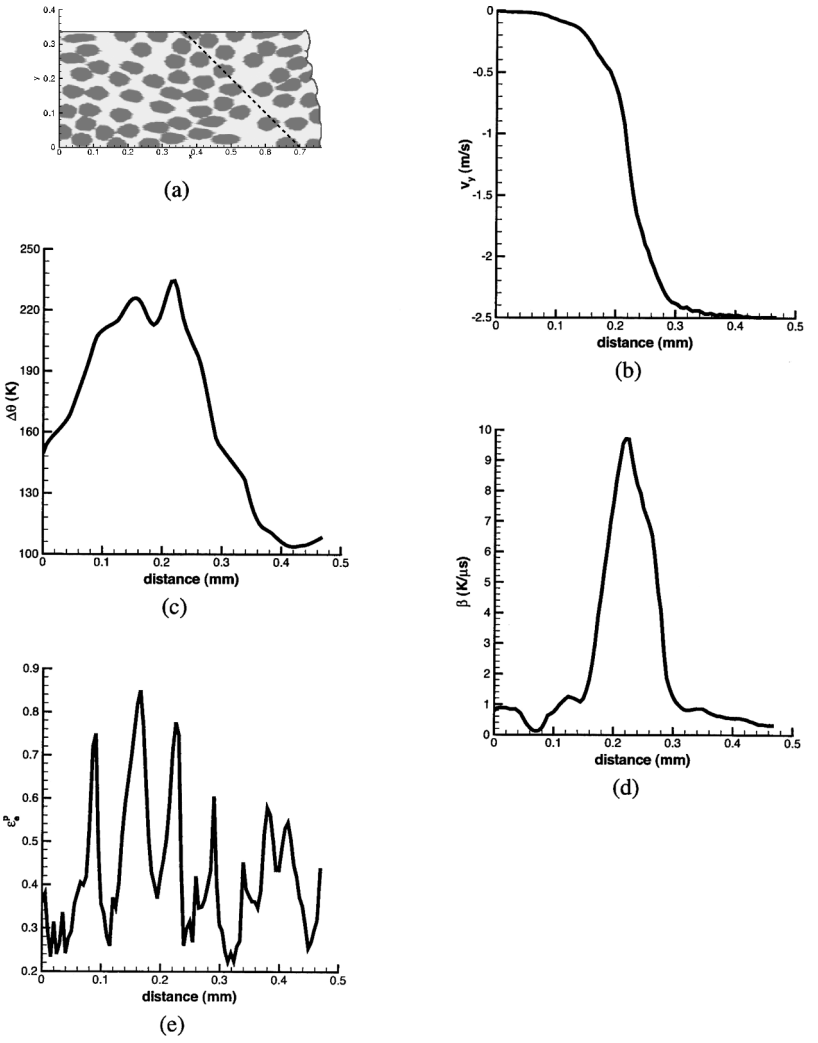

Figure 14 At time $t = 66.6\,\mu s$, (a) estimated centerline of ASB; (b)–(e) variation of the axial velocity, temperature rise, rate of temperature rise, and the effective plastic strain on a line perpendicular to the ASB. The distance is measured from the point $(0.7\,mm, 0)$.

Batra and Ko [53] scrutinized the effect of frictional force at the specimen/loading device interface during axisymmetric compression of a homogeneous thermoviscoplastic body containing a defect at its centroid. They refined the mesh adaptively in order to delineate an ASB. It was found that for smooth contact surfaces the specimen barreled inwards (i.e., the diameter of the deformed specimen at its center was less than that at its end faces) but it barreled outwards for the case of infinite friction. Also an ASB initiated much later in the axisymmetric problem than in the plane strain problem, and the rate of the axial load drop subsequent to the ASB initiation was considerably less for the axisymmetric deformations than that for the plane strain deformation.

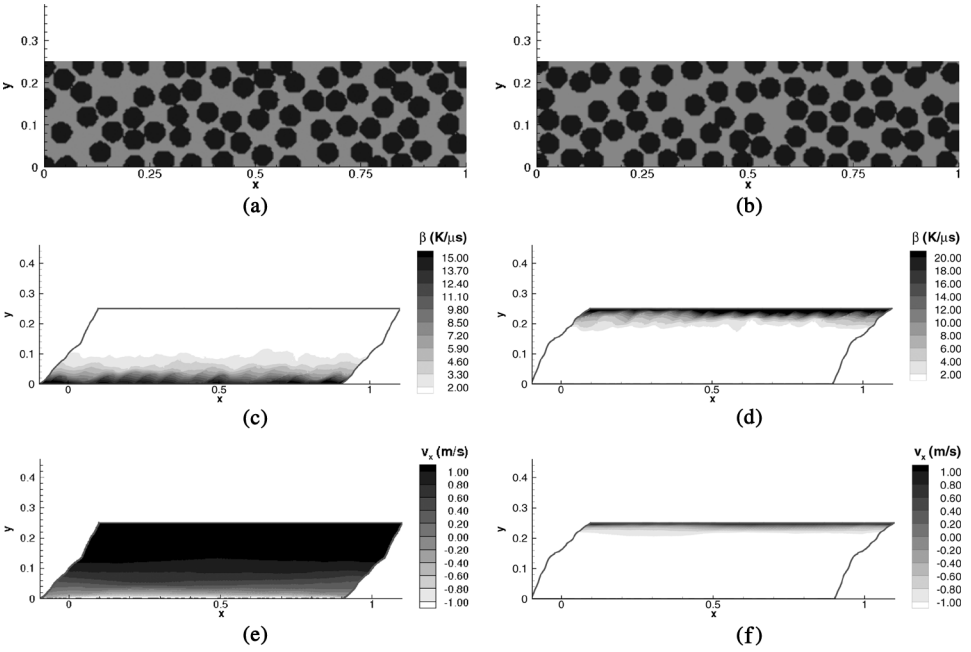

Figure 15 For the plane strain simple shear deformations of 50/50 W/NiFe particulate composite, (a) and (b) particulate arrangements; (c) and (d) fringe plots of the rate of temperature rise and (e) and (f) fringe plots of the velocity in the shearing direction.

Plane Strain Shear Deformations

We have analyzed plane strain simple shearing deformation of a 50/50 W/NiFe particulate composite deformed at a nominal strain rate of 5,000/s. Figure 15a,b exhibits the two particulate arrangements studied and the corresponding fringes of the velocity in the direction of shearing and the rate of temperature increase. Whereas for the particulate arrangement of Figure 15a the deformation localizes in the region abutting the bottom bounding surface, it does so near the top bounding surface for the particulate arrangement of Figure 15b; the corresponding times are 65 μs and 62 μs, respectively. Because of the periodic boundary conditions prescribed on the two vertical edges, no waves are reflected from them. However waves are reflected and refracted from the particulate/matrix interfaces and the top and the bottom bounding surfaces. Consequently the state of deformation within the body need not be that of simple shear. The speed of a shear (or a transverse) wave in W is 0.86 times that in NiFe. The two random particulate arrangements scrutinized are not symmetric about the midsurface of the specimen; accordingly, deformations are asymmetric about the midsurface.

Axisymmetric Compression

For smooth contact between the loading device and the specimen, and three random arrangements of particulates in a 50/50 W/NiFe composite, no ASB formed

Table 5 ASB initiation times for the different modes of deformation

Mode of deformation	ASB initiation time (μs)
Plane strain tension	56.4
Plane strain compression	66.6
Plane strain simple shear	63.5
Axisymmetric compression	>120.2
Axisymmetric tension	97

till $t = 120.2\,\mu s$. The axial velocity varied smoothly throughout the specimen. Computations ceased because of severe distortions of one of the elements in the FE mesh.

For axisymmetric tensile deformations, Figure 16a,b depicts contours of the rate of increase of temperature and the time history of its evolution at three points whose coordinates are given in the Figure. Material of the point initially at $(0.120, 0.030)$ is w and that of the other two points is NiFe. It is evident that the connected region with the high rate of increase of temperature is not straight as it is for the plane strain problem. Also, the constraint of axisymmetric deformations delays the formation of an ASB; a similar phenomenon was observed in a homogeneous body by Batra and Ko [53].

CONCLUSIONS

We have studied the development of an adiabatic shear band (ASB) in a particulate composite by analyzing deformations of the particulates and the matrix and also of the equivalent homogenized body. Plane strain tensile, plane strain compressive, plane strain simple shear and axisymmetric tensile/compressive deformations have been scrutinized. It is postulated that an ASB initiates at a point when the slope of the rate of temperature increase vs. time curve suddenly increases by an order of magnitude. For the 50/50 W/NiFe particulate composite the ASB initiation times for the three modes of deformation, obtained by averaging values listed in Table 4, are given in Table 5.

For plane strain compressive deformations of a particulate composite an ASB initiates even when the total axial load is monotonically increasing. Thus consideré criterion [56] cannot be used to discern when the structure will become unstable. The failure in plane strain compression is more sudden and hence more catastrophic than in plane strain tension.

It is found that the initiation and propagation of ASBs in particulate composites is decidedly different from that in a homogeneous material; particulate/matrix interfaces act as defects, introduce strong inhomogeneities into the deformations, and promote the formation of ASBs. The point from where an ASB originates and the shapes of regions where the deformations have localized strongly depend upon the arrangement of particulates, and their diameters. A decrease in the particulate diameter enhances the initiation of an ASB. Contours of the rate of change of temperature and of an appropriate component of velocity rather than contours of the effective plastic strain facilitate the delineation of ASBs. The ASB initiation criterion applicable to homogeneous and functionally graded materials fails for

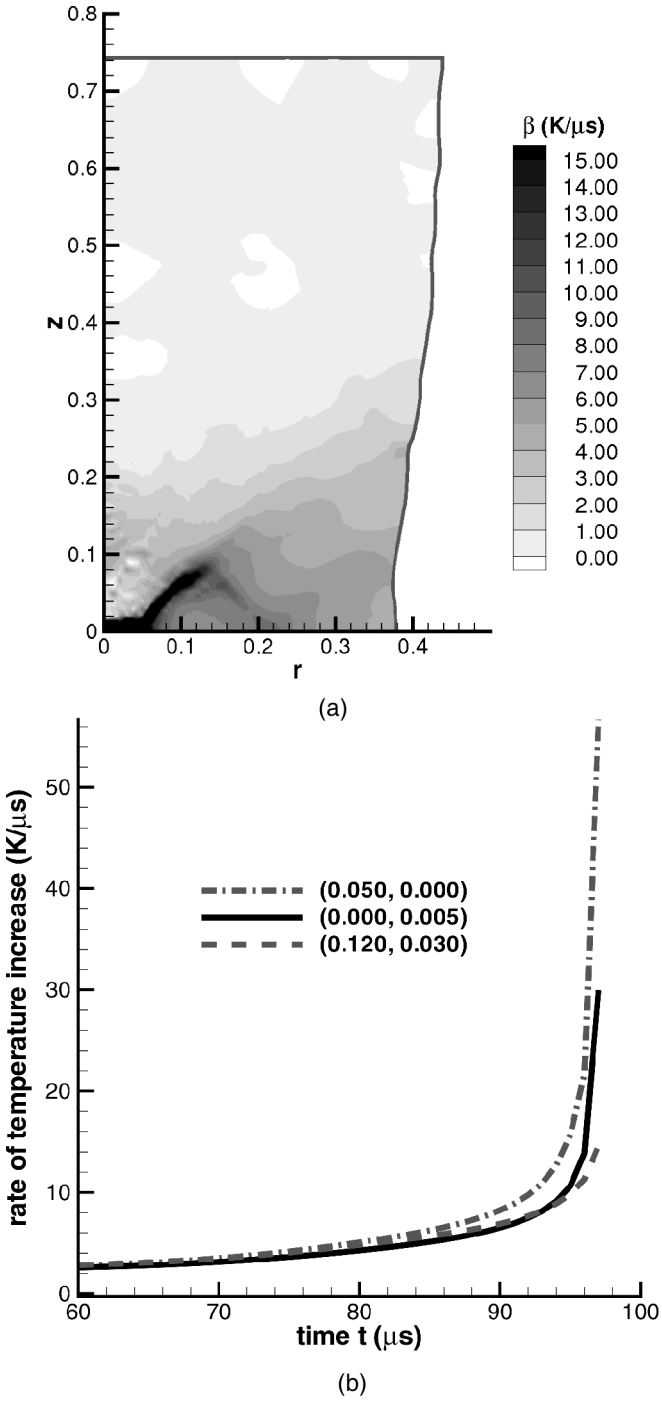

Figure 16 For axisymmetric tensile deformations, Figure 16a, b depicts contours of the rate of increase of temperature and the time history of its evolution at three points whose coordinates are given in the Figure. Material of the point initially at ($\phi.12\phi$, $\phi.\phi3\phi$;) is w and that of the other two points is Nife. It is evident that the connected region with the high rate of increase of temperature is not straight as it is for the plane strain problem, Also, the constraint of axisymmetric deformations delays the formation of an ASB; a similar phenomenon was observed in a homogeneous body by Batra and Ko [53].

Table 6 Comparison of ASB initiation and development in a homogeneous body and a particulate composite

Homogeneous body	Particulate composite
ASB originates from one point and propagates in the direction of the maximum shear stress.	ASB initiates at numerous points either simultaneously or sequentially and eventually may not pass through all of them.
Deformation becomes inhomogeneous either due to the presence of an artificial defect or due to the interaction among incident waves and waves reflected from boundaries.	Particulate/matrix interfaces introduce strong inhomogeneities in the deformation.
Contours of effective plastic strain can be used to discern an ASB.	Contours of the rate of temperature rise rather than of the effective plastic strain can be used to delineate an ASB.
In simple loadings the direction of an ASB can be predetermined.	The orientation of an ASB cannot be estimated.
Tangential velocity varies sharply across an ASB.	Tangential velocity varies sharply across an ASB.
ASB tip can be ascertained during the analysis.	ASB tip cannot be found during the analysis.
Effective plastic strain varies smoothly across an ASB.	Effective plastic strain need not vary smoothly across an ASB.
The load drops sharply when an ASB initiates in plane strain tensile deformations.	The load drops gradually in plane strain tensile deformations.
Once the ASB initiation criterion has been satisfied at a point, it stays within the ASB subsequently.	Once the ASB initiation criterion for a constituent has been satisfied at a point, it does *not* necessarily stay within the ASB subsequently.
The effective plastic strain is maximum at the ASB center.	The effective plastic strain is not necessarily maximum at the center of an ASB.

particulate composites. For plane strain tensile deformations, the time when the total axial load has dropped to 80% of its peak value indicates when the ASB has developed but provides no information about its point of initiation. For plane strain compressive deformations of a particulate composite an ASB initiates even when the total axial load is monotonically increasing. Thus Considerè criterion [56] can not be used to discern when the structure will become unstable. The failure in plane strain compression is more sudden and hence more catastrophic than that in plane strain tension. These and other differences/similarities between ASB development in homogeneous bodies and particulate composites are enumerated in Table 6.

In experiments one usually identifies a region of intense plastic deformation with an ASB. As fringe plots of Figures 3 and 5 and the variation of the effective plastic strain across an ASB in Figure 14 vividly illustrate there are numerous such regions. However, the regions of steep gradients in the velocity and the rate of temperature rise coincide with each other and do not necessarily encompass all regions of large effective plastic strain. The effective plastic strain rate and the specific energy dissipation rate in regions of high rate of increase of temperature are very large. Depending upon the magnitude of the applied load and its duration the deformed specimen may exhibit numerous regions of large plastic deformation without the formation of a coherent shear band. There is the possibility of several microshear bands forming within a macroshear band. An experimentalist has the daunting task of

delineating all these. The $5\,\mu m \times 5\,\mu m$ finite elements used in the analysis provide a good qualitative description of the deformation. One needs a significantly finer mesh to fully resolve all of the quantitative information, especially the band width. The ASB initiation time decreases with a decrease in the particulate diameter. For the three random particulate arrangements of 50% by volume of $50\,\mu m$ diameter W particulates in NiFe matrix, the ASB initiation times varied by less than 10%.

Finally we note that the bounding surface for all of the problems studied have been taken to be thermally insulated. Batra and Wei [57] have scrutinized the initiation and development of shear bands due to heat flux prescribed at the end faces in an elasto thermoviscoplastic body undergoing simple shearing deformations.

REFERENCES

1. Y. L. Bai and B. Dodd, *Adiabatic Shear Localization: Occurence, Theories, and Applications*, Pergamon Press, Oxford, 1992.
2. T. W. Wright, *The Physics and Mathematics of Adiabatic Shear Bands*, Cambridge University Press, Cambridge, 2002.
3. P. Perzyna (ed.), *Localization and Fracture Phenomenon in Inelastic Solids*, Springer-Verlag, 1998.
4. R. C. Batra and H. M. Zbib (eds.), *Material Instabilities: Theory and Applications*, ASME Press, 1994.
5. Y. Tomita, Simulation of Plastic Instabilities in Solid Mechanics, *Appl. Mechs. Revs.*, vol. 47, pp. 171–205, 1994.
6. R. Armstrong, R. C. Batra, M. Meyers, and T. W. Wright, Shear Instabilities and Viscoplasticity Theories, *Mechs. of Materials*, vol. 17, pp. 83–328, 1994.
7. R. C. Batra, Y. D. S. Rajapakse, and A. Rosakis, Failure Mode Transitions Under Dynamic Loading, *Int. J. of Fracture*, vol. 101, pp. 1–180, 2000.
8. H. M. Zbib, T. Shawki, and R. C. Batra, Material Instabilities, *Appl. Mech. Rev.*, vol. 45, pp. 1–173, 1992.
9. R. C. Batra and B. M. Love, Adiabatic Shear Bands in Functionally Graded Materials, *J. Thermal Stresses*, vol. 27, pp. 1101–1123, 2004.
10. M. Zhou, A. Needleman, and R. J. Clifton, Finite Element Simulations of Dynamic Shear Localization, *J. Mech. Phys. Solids*, vol. 42, pp. 423–458, 1994.
11. M. Zhou and R. J. Clifton, Dynamic Constitutive and Failure Behavior of a Two-Phase Tungsten Composite, *J. Appl. Mech.*, vol. 64, pp. 487–494, 1997.
12. A. Bose, H. Congue, and J. Lankford Jr., Influence of Microstructure on Shear Localization in Tungsten Heavy Alloys, in A. Bose and R. J. Dowding (eds.), *Proceedings of the First International Conference on Tungsten and Tungsten Alloys*, pp. 291–298, November 15–18, Metal Powder Industries Federation, Arlington, VA, 1992.
13. D. K. Kim, S. Lee, and H. S. Song, Effect of Tungsten Particle Shape on Dynamic Deformation and Fracture Behavior of Tungsten Heavy Alloys, *Metall. Mater. Trans. A*, vol. 29, pp. 1057–1069, 1998.
14. Z. Wei, J. Yu, J. Li, Y. Li, and S. Hu, Influence of Stress Condition on Adiabatic Shear Localization of Tungsten Heavy Alloys, *Int. J. Impact Eng.*, vol. 26, pp. 843–852, 2001.
15. R. D. Dick, V. Ramachandran, J. D. Williams, R. W. Armstrong, W. H. Holt, and W. Mock, Jr., Dynamic Deformation of W7Ni3Fe Alloy via Reverse-Ballistic Impact, in A. Crowson and E. S. Chen (eds.), *Tungsten and Tungsten Alloys–Recent Advances*, pp. 269–276, The Minerals, Metals & Materials Society, 1991.
16. J. B. Stevens and R. C. Batra, Adiabatic Shear Bands in the Taylor Impact Test for a WHA Rod, *Int. J. Plasticity*, vol. 14, pp. 841–854, 1998.

17. R. C. Batra and J. B. Stevens, Adiabatic Shear Bands in Axisymmetric Impact and Penetration Problems, *Computer Methods in Appl. Mechs. and Eng'g.*, vol. 151, pp. 325–342, 1998.
18. R. C. Batra and N. M. Wilson, Adiabatic Shear Bands in Plane Strain Deformations of a WHA, *Int. J. Plasticity*, vol. 14, pp. 43–60, 1998.
19. M. Zhou, The Growth of Shear Bands in Composite Microstructures, *Int. J. Plasticity*, vol. 14, pp. 733–754, 1998.
20. N. Charalambakis and T. Baxevanis, Adiabatic Shearing of Non-Homogeneous Thermoviscoplastic Materials, *Int. J. Plasticity*, vol. 20, pp. 899–914, 2004.
21. R. C. Batra and N. A. Jaber, Failure Mode Transition in an Impact Loaded Prenotched Plate with Four Thermoviscoplastic Relations, *Int. J. Fracture*, vol. 110, pp. 47–71, 2001.
22. A. L. Gurson, Continuum Theory of Ductile Rupture by Void Nucleation and Growth: Part I, *J. of Engr. Mater. and Tech.*, vol. 99, pp. 2–15, 1977.
23. V. Tvergaard, Influence of Voids on Shear Band Instabilities Under Plane Strain Conditions, *Int. J. Fracture*, vol. 17, pp. 389–407, 1981.
24. G. R. Johnson and W. H. Cook, A Constitutive Model and Data for Metals Subjected to Large Strains, High Strain-Rates, and High Temperatures, *Proc. 7th Int'l. Symp. on Ballistics*, pp. 541–547, 1983.
25. C. Chu and A. Needleman, Void Nucleation in Biaxially Stretched Sheets, *J. Engr. Mat. Tech.*, vol. 102, pp. 249–256, 1980.
26. V. Tvergaard and A. Needleman, Analysis of the Cup-Cone Fracture in a Round Tensile Bar, *Acta Metallurgica*, vol. 32, pp. 157–169, 1984.
27. B. Budiansky, Thermal and Thermoelastic Properties of Isotropic Composites, *J. Composite Materials*, vol. 4, pp. 701–744, 1990.
28. C. Cattaneo, A Form of the Heat Equation which Eliminates the Paradox of Instantaneous Propagation, *CR Acad. Sci.*, vol. 247, pp. 431–433, 1958.
29. P. Vernotte, The True Heat Equation, *CR Acad. Sci.*, vol. 247, p. 2103, 1958.
30. R. C. Batra and M. H. Lear, Adiabatic Shear Banding in Plane Strain Tensile Deformations of 11 Thermoviscoplastic Materials with Finite Wave Speed, *Int. J. Plasticity*, vol. 21, pp. 1521–1545, 2005.
31. R. C. Batra and L. Chen, Instability Analysis and Shear Band Spacing in Gradient-Dependent Thermoviscoplastic Materials with Finite Speeds of Thermal Waves, *Archives of Mechanics*, vol. 53, pp. 167–192, 2001.
32. R. C. Batra, On Heat Conduction and Wave Propagation in Non-Simple Rigid Solids, *Letters in Appl. and Engng. Sci.*, vol. 3, pp. 97–107, 1975.
33. R. C. Batra and C. H. Kim, Effect of Viscoplastic Flow Rules on the Initiation and Growth of Shear Bands at High Strain Rates, *J. Mech. Phys. Solids*, vol. 38, pp. 859–874, 1990.
34. R. C. Batra and L. Chen, Effect of Viscoplastic Relations on the Instability Strain, Shear Band Initiation Strain, the Strain Corresponding to Maximum Shear Band Spacing, and the Band Width in a Thermoviscoplastic Material, *Int. J. Plasticity*, vol. 17, pp. 1465–1489, 2001.
35. R. C. Batra, Steady State Penetration of Thermoviscoplastic Targets, *Comp. Mechs.*, vol. 3, pp. 1–12, 1988.
36. S. R. Bodner and Y. Partom, Constitutive Equations for Elastic-Viscoplastic Strain-Hardening Materials, *J. Appl. Mech.*, vol. 56, pp. 385–389, 1975.
37. T. J. R. Hughes, *The Finite Element Method, Linear Static and Dynamic Finite Element Analysis*, Prentice Hall, Englewood Cliffs, 1987.
38. R. C. Batra and D. Rattazzi, Adiabatic Shear Banding in a Thick-Walled Steel Tube, *Comp. Mechs.*, vol. 20, pp. 412–426, 1997.
39. A. Marchand and J. Duffy, An Experimental Study of the Formation Process of Adiabatic Shear Bands in a Structural Steel, *J. Mechs. Phys. Solids*, vol. 36, pp. 251–283, 1988.

40. R. C. Batra and C. H. Kim, Analysis of Shear Bands in Twelve Materials, *Int. J. Plasticity*, vol. 8, pp. 425–452, 1992.
41. R. C. Batra, Finite Plane Strain Deformations of Rubberlike Materials, *Int. J. Numer. Meth. Eng'g.*, vol. 15, pp. 145–160, 1980.
42. R. C. Batra and X. Q. Liang, Finite Deformations of Smart Structures, *Comp. Mechs.*, vol. 20, pp. 427–438, 1997.
43. R. C. Batra and B. M. Love, Crack Propagation due to Brittle and Ductile Failures in Microporous Thermoelastoviscoplastic Functionally Graded Materials, *Engineering Fracture Mechanics*, (in press).
44. T. C. Chiu and F. Erdogan, One-Dimensional Wave Propagation in a Functionally Graded Medium, *J. Sound and Vibration*, vol. 222, pp. 453–487, 1999.
45. A. Molinari and R. J. Clifton, Analytical Characterization of Shear Localization in Thermoviscoplastic Materials, *J. Appl. Mech.*, vol. 54, pp. 806–812, 1987.
46. B. M. Love and R. C. Batra, Determination of Effective Thermomechanical Parameters of a Mixture of Two Elastothermoviscoplastic Constituents. (to be submitted).
47. L. H. Dai, L. F. Liu, and Y. L. Bai, Formation of Adiabatic Shear Bands in Metal Matrix Composites, *Int. J. Solids and Structures*, vol. 41, pp. 5979–5993, 2004.
48. R. C. Batra, The Initiation and Growth of, and the Interaction Among Adiabatic Shear Bands in Simple and Dipolar Materials, *Int. J. Plasticity*, vol. 3, pp. 75–89, 1987.
49. R. C. Batra and C. H. Kim, Adiabatic Shear Banding in Elastic-Viscoplastic Nonpolar and Dipolar Materials, *Int. J. Plasticity*, vol. 6, pp. 127–141, 1990.
50. R. C. Batra and C. H. Kim, The Interaction Among Adiabatic Shear Bands in Simple and Dipolar Materials, *Int. J. Engng. Sci.*, vol. 28, pp. 927–942, 1990.
51. Y. W. Kwon and R. C. Batra, Effect of Multiple Initial Imperfections on the Initiation and Growth of Adiabatic Shear Bands in Nonpolar and Dipolar Materials, *Int. J. Engng. Sci.*, vol. 26, pp. 1177–1187, 1988.
52. R. C. Batra and Y. W. Kwon, Adiabatic Shear Banding in a Bimetallic Body, *Acta Mechanica*, vol. 77, pp. 281–297, 1989.
53. R. C. Batra and K. I. Ko, Analysis of Shear Bands in Dynamic Axisymmetric Compression of a Thermoviscoplastic Cylinder, *Int. J. Engng. Sci.*, vol. 31, pp. 529–547, 1993.
54. R. C. Batra, Effect of Material Parameters on the Initiation and Growth of Adiabatic Shear Bands, *Int. J. Solids and Structures*, vol. 23, pp. 1435–1446, 1987.
55. R. C. Batra and J. Hwang, Dynamic Shear Band Development in Dipolar Thermoviscoplastic Materials, *Computational Mechs.*, vol. 12, pp. 354–369, 1994.
56. A. G. Considerè, Memiore Sur L'emploi du fer et de L'acier dans les constructions, Annals des Pontset Chaussees, vol. 9, pp. 574–775, 1885.
57. R. C. Batra and Z. G. Wei, Shear Bands Due to Heat Flux Prescribed at Boundaries, *Int. J. Plasticity* (in press, available online).